European Journal of Mechanics / B Fluids 70 (2018) 46–72

Contents lists available at ScienceDirect

European Journal of Mechanics / B Fluids

journal homepage: www.elsevier.com/locate/ejmflu

# Computation of fluid flow in double sided cross-shaped lid-driven cavities using Lattice Boltzmann method

Sthavishtha Bhopalam R., D. Arumuga Perumal *, Ajay Kumar Yadav

*Department of Mechanical Engineering, National Institute of Technology Karnataka, Surathkal, Mangalore 575025, India*

## HIGHLIGHTS

- Application of LBM to compute flow in double sided cross-shaped lid-driven cavities.
- Uniform antiparallel/parallel motion analysis carried out for first time by LBM.
- Oscillating antiparallel/parallel wall motion study carried out.
- Study of vortex dynamics, symmetry and anti-symmetry of the streamline patterns.
- Effect of Reynolds numbers and oscillating frequencies have been studied.

## ARTICLE INFO

*Article history:*
Received 22 August 2016
Received in revised form 22 November 2017
Accepted 30 January 2018
Available online 19 February 2018

*Keywords:*
Double-sided cross-shaped lid-driven cavity
Lattice Boltzmann method
Two relaxation time
Antiparallel wall motion
Parallel wall motion
Oscillating lid

## ABSTRACT

This work implements Lattice Boltzmann method to compute flows in double-sided cross-shaped lid-driven cavities. Firstly, a complicated geometry which is a symmetrized version of the staggered lid-driven cavity namely, the double-sided cross-shaped lid-driven cavity with antiparallel uniform wall motion is studied employing Single as well as Two Relaxation time models. The streamline patterns and vorticity contours obtained for low to moderate Reynolds numbers (150–1000) are compared with published results and found to be in good accordance. Next, this code is extended to simulate flows in a double-sided cross-shaped lid-driven cavity with parallel uniform wall motion. The effect of three dimensionality is also studied for low Reynolds numbers. Lattice Boltzmann method is then used to investigate the oscillating double-sided cross-shaped lid-driven cavity with antiparallel and parallel wall motions. The movement and formation of primary and secondary vortices have been well captured with the variation of Reynolds numbers and oscillating frequencies for uniform and oscillating wall motions. Reasonable agreements with the established results have been observed for the double-sided cross-shaped cavity with uniform wall motions, while new results have been obtained in the case of oscillating wall motions.



## 1. Introduction

Fluid dynamics simulation by numerical techniques has been the principal research topic for the past few decades [1,2]. With the birth of Computational Fluid Dynamics (CFD) as an area utilizing the computational resources to solve the governing equations of fluid mechanics, tremendous growth in the development of numerical algorithms has been observed lately. To establish the accuracy and computational efficiency of such algorithms, it becomes necessary to compute flows in benchmark geometries like lid driven cavity, which is being widely adopted [3]. Its preference over existing benchmark problems could be attributed to its capability in exhibiting all possible phenomena in incompressible flows like eddies, secondary flows, chaotic particle motions, instabilities, transition and turbulence [4]. These characteristic flow features have resulted in its industrial and academic applications like coating [5] and drying, melt spinning processes, mixing [6], aerodynamics [7] and slots of heat exchanger cut-outs. Additionally, three-dimensional end wall effects on cubic cavity flows have been found even at large aspect ratios [8,9]. The aforementioned features associated with lid driven cavity flows have made it a remarkable benchmark problem, motivating further research in this area. This has been substantiated by successful studies in several shapes of cavities like, L-shaped [10,11], T-shaped [12,13], C-shaped [14], trapezoidal [15], semi-circular [16,17], cross shaped etc.

The lid driven cavity's ability to test the accuracy and efficiency of modern developed numerical schemes, coupled with its intrinsic popularity has sparked several investigations in the literature. Initial numerical studies were dedicated to two-dimensional lid driven cavities [18]. Additionally, precise computations in such configurations were established by Ghia et al. [19], who implemented a stream-function vorticity approach along with a coupled

* Corresponding author.
*E-mail address:* perumal@nitk.edu.in (D.A. Perumal).

https://doi.org/10.1016/j.euromechflu.2018.01.006
0997-7546/

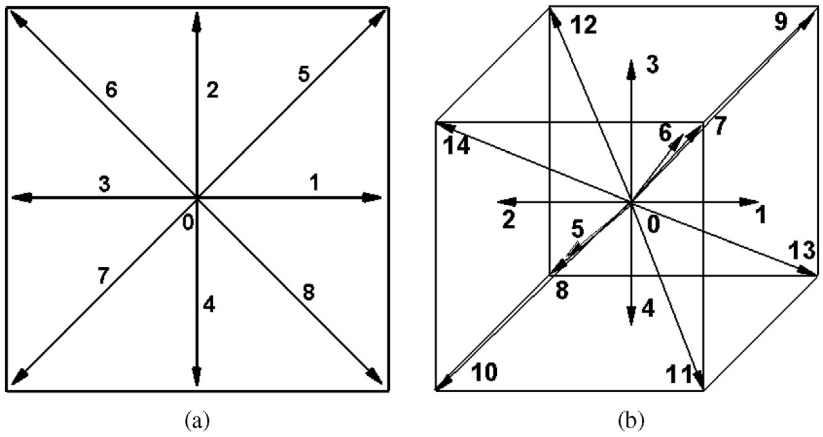


**Fig. 1.** Lattice models (a) *D2Q*9 and (b) *D3Q* 15.

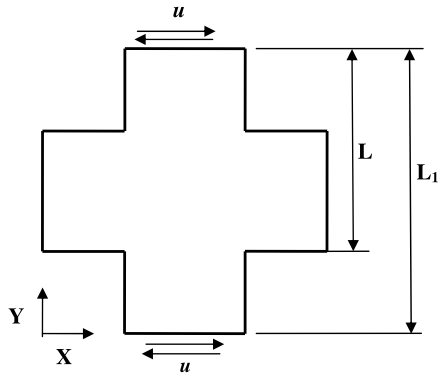


**Fig. 2.** Geometry of the double sided cross-shaped cavity.

implicit multigrid method. Though the above studies were limited to square cavities with unity aspect ratios, rectangular cavities with various aspect ratios were also studied [20,21]. The single lid-driven cavity problems were later extended to the case of double sided lid-driven cavities by Kuhlmann et al. [22]. A similar study incorporating parallel and antiparallel wall motions in the same cavity configuration was conducted by Perumal and Dass [23]. Further, three-dimensional cavity flows have also been studied earlier, for demonstrating complex and realistic flows in nature. The three-dimensionality effect leads to slight deviations from the two-dimensional cavity flow results, due to the formation of boundary layer across the side walls. Previous reliable studies [24,25] have been investigated in this direction. Additionally, some numerical studies for three-dimensional flows have been performed using Lattice Boltzmann Method [26,27].

Apart from the steady flows mentioned earlier, unsteady flows have also been explored, owing to its practicality. In such cases, the unsteady flows have been simplified by assuming the velocity to oscillate in accordance with a fixed amplitude and angular frequency. In the realm of experiments, Sriram et al. [28] adopted experimental particle image velocimetry techniques (PIV) to study the variation of fluid flow in an oscillating lid driven cavity over a wide range of Reynolds numbers from 5 to 3700. Subsequently, they obtained a qualitative and quantitative understanding of the flow behaviour in a glycerol–water solution using 2-D and 3-D simulations respectively. On the other hand, numerical methods like Smoothed Particle Hydrodynamics (SPH) [29], Finite Difference Method (FDM) [30] and stream function vorticity approach [31] were used to study similar phenomenon in the area of numerical techniques. Moreover, Noor et al. [32] analysed the fluid flow and

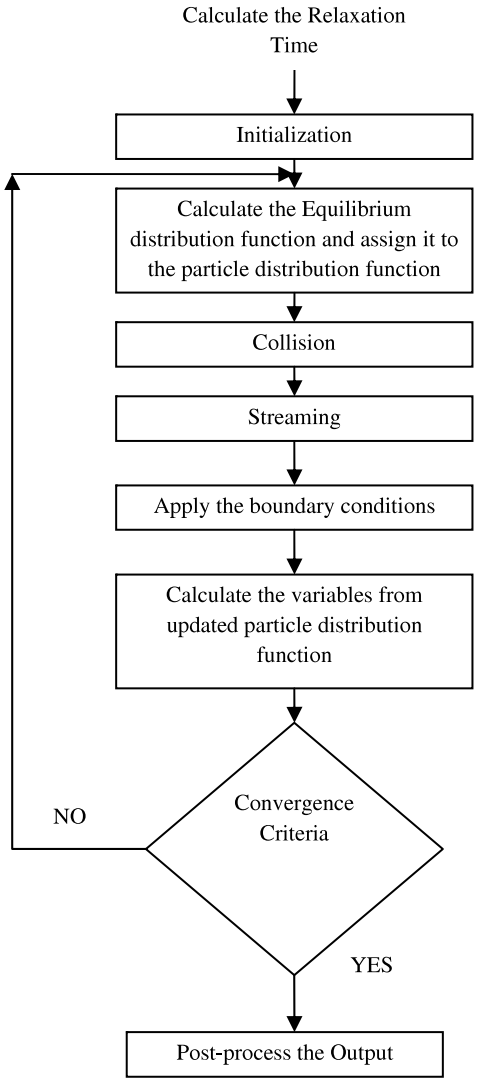


**Fig. 3.** Flow chart of lattice Boltzmann method.

heat transfer characteristics in double sided oscillating cavities, using QUICK and central differencing schemes. A pioneering study by Nishimura and Kunitsugu [33] showed that oscillating frequencies and aspect ratios were the important parameters responsible for controlling fluid mixing in such conditions. In this direction,

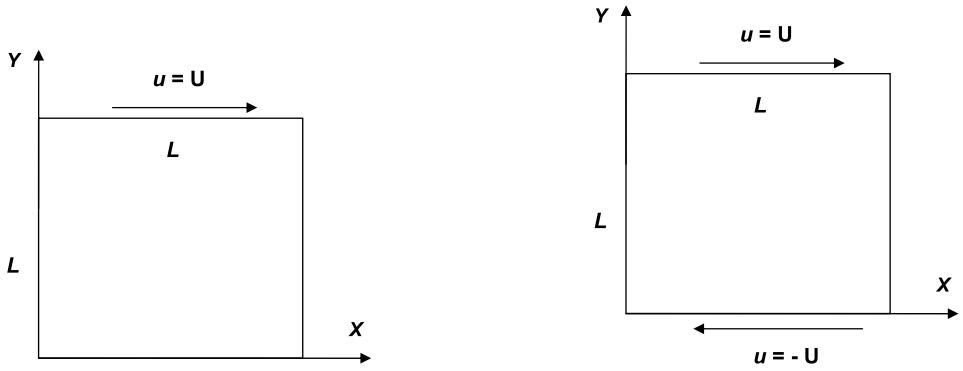


**Fig. 4.** Geometry of the square cavities considered for code validation.

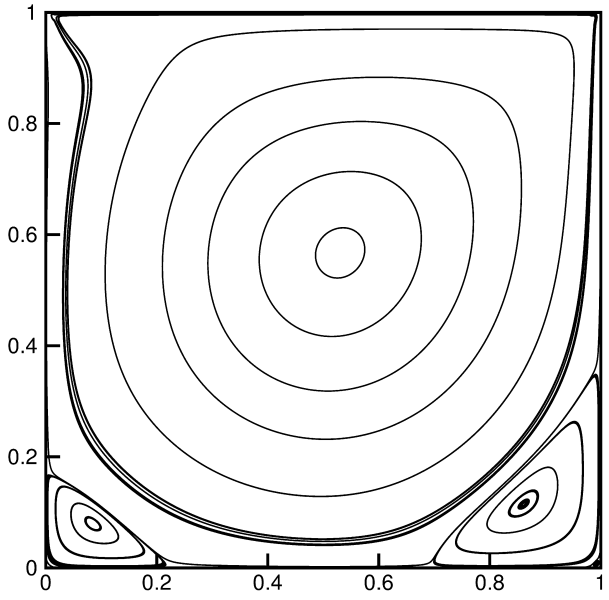


**Fig. 5.** Streamlines in the single sided square cavity at $Re = 1000$.

Takasaki et al. [34] observed that oscillating frequency predominantly enhanced the fluid mixing, and the role of other parameters were negligible for a range of Reynolds numbers from 50 to 500. Recently, Lattice Boltzmann Method was also implemented to study oscillating flows in single-sided oscillating square cavities by Mendu and Das [35], to demonstrate the effectiveness of this numerical method over its counterparts.

Despite the wide usage of FDM and Finite Volume Methods (FVM) in CFD as a part of the conventional Navier–Stokes (N–S) solvers [36], they have a fundamental drawback associated with the pressure (Poisson equation) solver. This has been overcome by several mesoscopic approaches, with Lattice Boltzmann Method (LBM) being one among the popular ones. Having grown out of Lattice Gas Models (LGM), LBM tracks the distribution of particles unlike the macroscopic approaches which solve the N–S equations. Its popularity can be attributed to its numerical stability, computational efficiency, simplicity and parallelizability (local computations) over existing CFD techniques. LBM has found significant applications [3] in microflows, nanofluids, compressible flows, multiphase, magneto hydrodynamics, heat transfer, turbulent flows, porous media, immiscible fluids, wave propagations, ocean circulations, fluid–structure interactions (FSI) and combustion.

LBM with Single Relaxation Time (LBM-SRT) is a commonly used simulation technique for incompressible flows [7]. Apart from LBM-SRT adopted in several studies, other variations of LBM, like

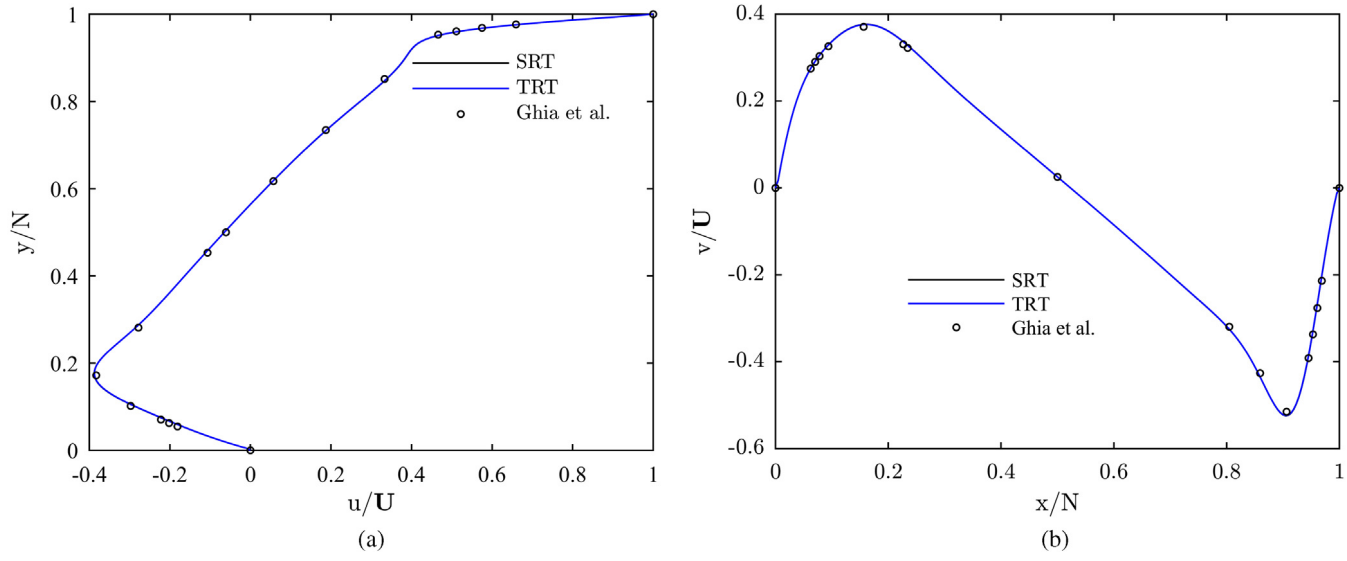


**Fig. 6.** Comparisons of predicted centreline velocity profiles with published results (a) $u$-velocity (b) $v$-velocity at $Re = 400$.

**Table 1**
Location of vortices in the cross-shaped cavity with antiparallel motion, for various lattice sizes.

| Lattice Size | Top primary vortex | | Bottom primary vortex | | Secondary vortex on the left | | Secondary vortex on the right | |
|---|---|---|---|---|---|---|---|---|
| | $x$ | $y$ | $x$ | $y$ | $x$ | $y$ | $x$ | $y$ |
| 176 × 176 | 0.7249 | 1.1794 | 0.6895 | 0.2339 | 0.4628 | 0.7298 | 0.9883 | 0.6825 |
| 281 × 281 | 0.7237 | 1.1770 | 0.6874 | 0.2343 | 0.4428 | 0.7294 | 0.9684 | 0.6819 |
| 561 × 561 | 0.7222 | 1.1750 | 0.6867 | 0.2350 | 0.4420 | 0.7280 | 0.9750 | 0.6750 |

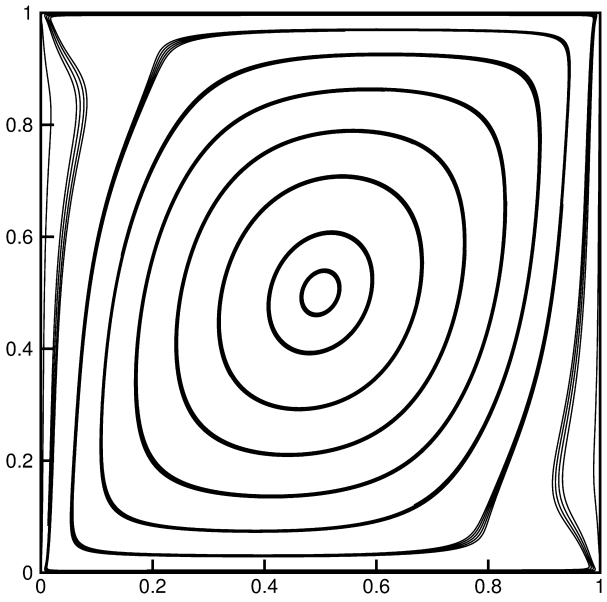


**Fig. 7.** Streamlines in a double sided square cavity with antiparallel motion at $Re = 400$.

Multi Relaxation Time (LBM-MRT) [37] and Two Relaxation Time (LBM-TRT) [38] have also been implemented in lid driven cavity flows. Presence of numerical instabilities is an inherent feature of LBM-SRT, which restricts its implementation to low Reynolds number flows. However, adoption of MRT has been found to solve this problem, resulting in stable solutions in the case of lid driven cavity flows [39]. Two-Relaxation Time model (TRT), a subset of Multiple Relaxation Time (MRT) model uses only two relaxation times and possesses similar characteristics as MRT. However, it is computationally less expensive over MRT as it uses only two relaxation times. The aforementioned models work well for uniform and moderately complex geometries. However, for intricately complex geometries, it becomes important to adopt alternative approaches like Taylor-series expansion and Least-squares-based LBM (TLLBM) [40], Interpolation-Supplemented Lattice Boltzmann Method (ISLBM) [41], and Immersed Boundary Lattice Boltzmann Method (IBLBM) [42].

Double-sided cross shaped lid driven cavity with uniform antiparallel wall motion was initially proposed and discussed by Vicente et al. [43]. A two-dimensional stability analysis was carried out for the same problem by Gogoi and Kalita [44]. This work was later extended by Gogoi [45], who carried out a global two-dimensional stability analysis in the same configuration for parallel and antiparallel wall motions. On the other hand, numerical works concerning flows in staggered lid driven cavities (antisymmetric versions of the cross-shaped configuration, with the top and bottom cavities diagonally offset) have also been successfully performed by Zhou et al. [46], Nithiarasu and Liu [47], Kalita and Gogoi [48] and Tekic et al. [49].

From this extensive review, we find that only few works using continuum-based methods have been carried out concerning numerical simulations in double sided cross-shaped lid-driven cavities, and no efforts have been made to compute flows in this configuration using LBM. This was the motivation behind the present work, to compute steady and oscillating behaviour in this configuration. Attempt has also been made to compare flow behaviour in the cross-shaped cavity with its antisymmetric counterpart staggered lid-driven cavity, as the latter has been a benchmark

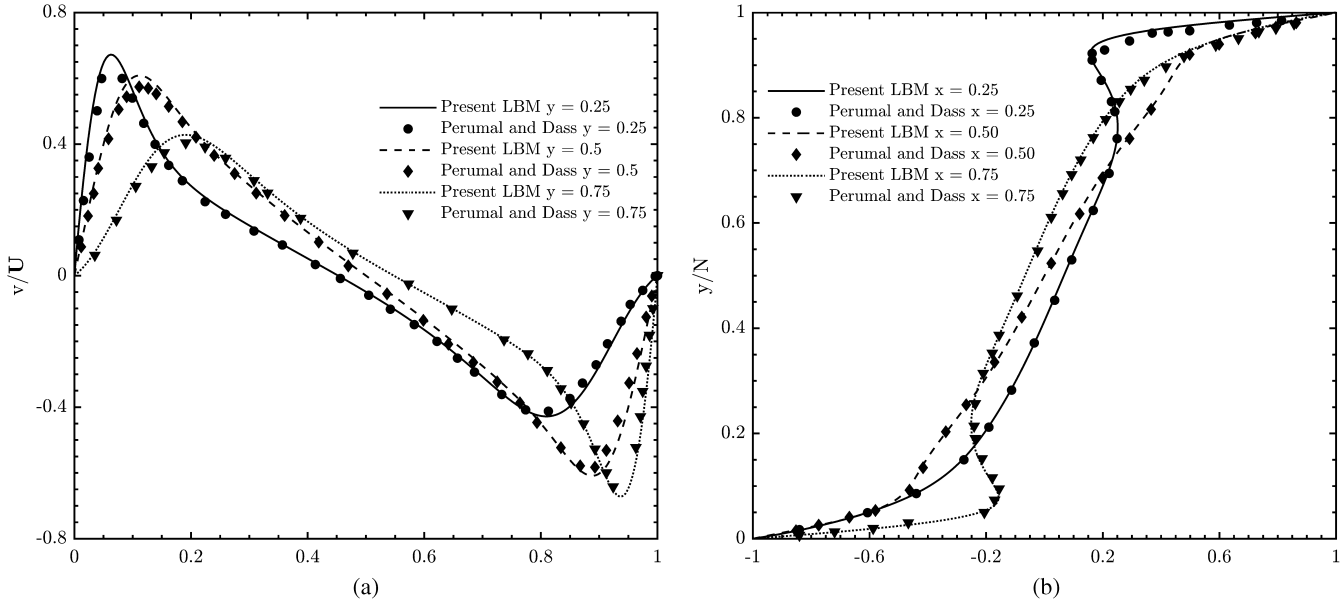


**Fig. 8.** Comparisons of predicted centreline velocity profiles with published results (a) $u$-velocity (b) $v$-velocity at $Re = 400$.

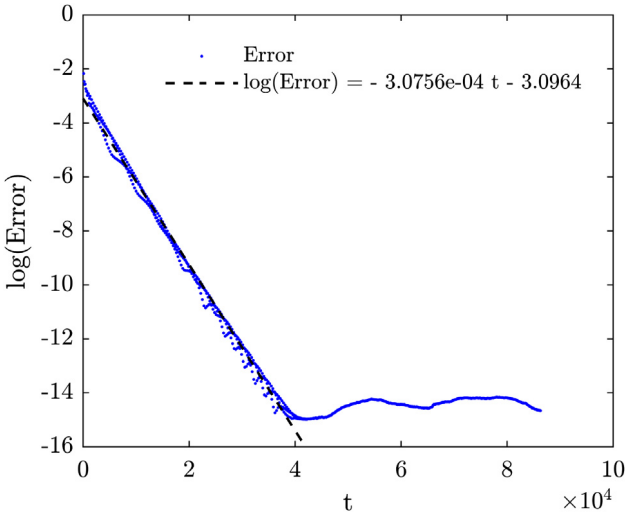


(a) $Re = 200$, SRT.

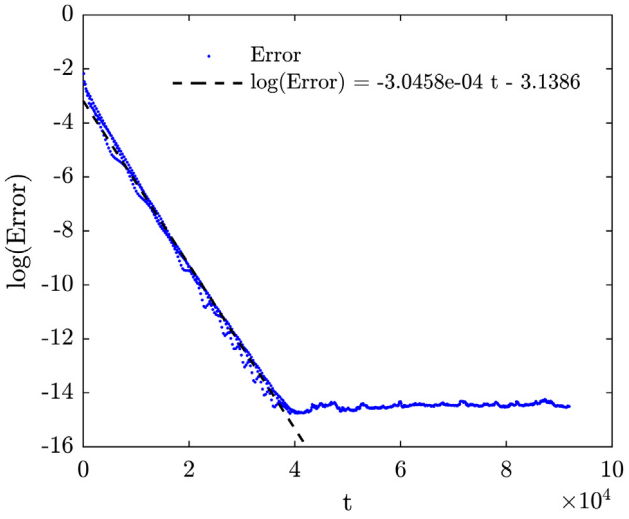


(b) $Re = 200$, TRT.

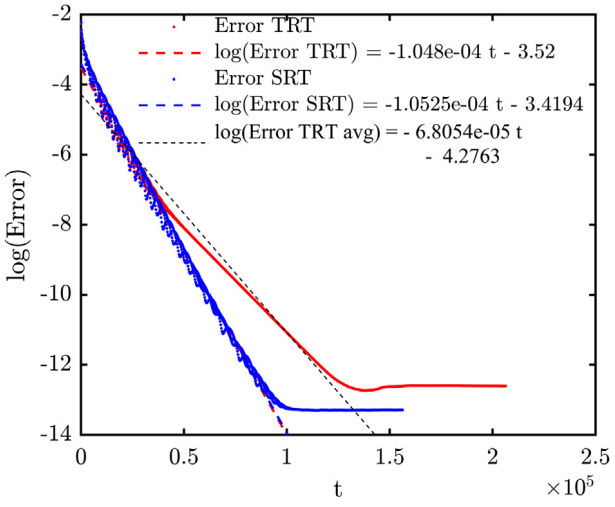


(c) $Re = 1000$, SRT and TRT.

**Fig. 9.** Temporal convergence history of the residual errors obtained in the cross-shaped cavity at antiparallel wall motion.

**Table 2**
Variation of longitudinal velocity components with the lattice velocities.

| $U$ | $(v/U)_{min}$ | $(v/U)_{max}$ |
|---|---|---|
| 0.05 | −0.6460 | 0.6460 |
| 0.1 | −0.6450 | 0.6450 |

problem in this area. Additionally, the results of TRT and SRT models are compared through the residual plots, to determine the optimum model to be used in the name of numerical stability and computational expenses. To give an insight to the reader about the effect of boundary layer, three-dimensional simulations have also been carried out in the same cavity configuration for the case of uniform wall motions only.

The current paper is categorized into five sections. Section 1 briefly reviewed relevant literature of this work. Section 2 explains the procedure of implementing LBM to fluid flow problems using two-dimensional nine ($D2Q9$) and three-dimensional fifteen velocity ($D3Q15$) models used in the adopted geometry. In Section 3, the double sided antiparallel uniform wall motion results are compared with the published works. With this established confidence in the developed numerical code, results of uniform parallel and oscillating wall motions are later studied. Finally, the conclusions of this work are summarized in Section 4.

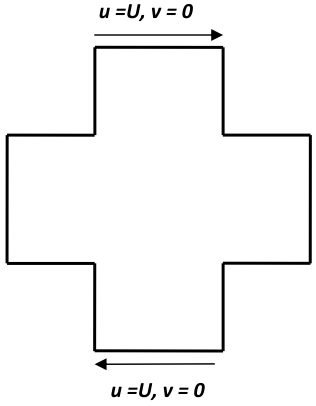


**Fig. 10.** Schematic representation of double sided cross shaped cavity with antiparallel uniform wall motion.

## 2. Numerical technique and problem description

### 2.1. Lattice Boltzmann method formulation

For the Single-Relaxation-Time model (SRT) of Lattice Boltzmann Method, the discrete Boltzmann equation can be written

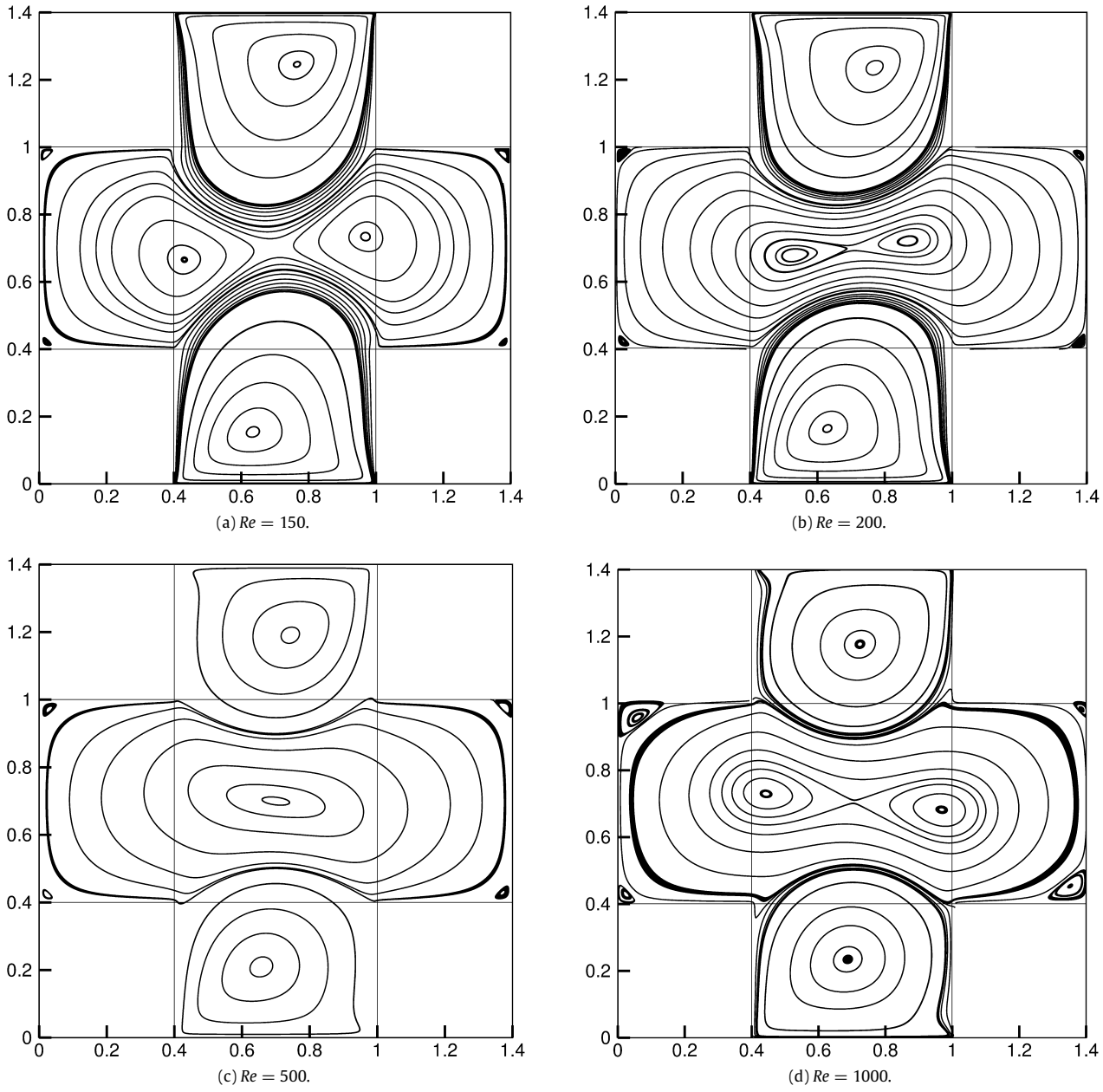


**Fig. 11.** Streamline patterns for double sided antiparallel wall uniform motion by present LBM at (a) $Re = 150$, (b) $Re = 200$, (c) $Re = 500$ and (d) $Re = 1000$.

as [50]:

$$f_\alpha\left(\mathbf{x}+\ \mathbf{c}_\alpha\Delta t,\ t+\Delta t\right)=f_\alpha\left(\mathbf{x},t\right)-\frac{1}{\tau}\left[f_\alpha\left(\mathbf{x},t\right)-{f_\alpha}^{eq}(\mathbf{x},t)\right] \quad (1)$$

where $\tau$ is the relaxation time related to the kinematic viscosity and $\alpha$ varies from 0–8 and 0–14 for $D2Q9$ and $D3Q15$ models respectively. Furthermore, $f_\alpha\left(\mathbf{x},t\right)$ and $f_\alpha^{eq}\left(\mathbf{x},t\right)$ are the particle and equilibrium distribution functions associated with the discrete lattice velocity $e_\alpha$ at $(\mathbf{x},t)$.

As mentioned earlier, a Two-Relaxation Time (TRT) model has been additionally adopted for comparison with SRT. The discrete Boltzmann equation in this case can be rewritten as [38]:

$$f_\alpha\left(\mathbf{x}+c_\alpha\Delta\mathrm{t},\ \mathrm{t}+\Delta\mathrm{t}\right)=f_\alpha\left(\mathbf{x},t\right)-\frac{1}{\tau^+}\left[{f_\alpha}^+\left(\mathbf{x},t\right)-{f_\alpha}^{eq,+}\left(\mathbf{x},t\right)\right]-\frac{1}{\tau^-}\left[{f_\alpha}^-\left(\mathbf{x},t\right)-{f_\alpha}^{eq,-}\left(\mathbf{x},t\right)\right] \quad (2)$$

where $\tau^+$ and $\tau^-$ refer to the symmetrical and anti-symmetrical relaxation times, whose relations are expressed later. The symmetrical and anti-symmetrical components of the distribution function can be computed as shown in Eq. (3).

$${f_\alpha}^+=\frac{f_\alpha+f_{\overline{\alpha}}}{2},\ {f_\alpha}^-=\frac{f_\alpha-f_{\overline{\alpha}}}{2} \quad (3)$$

where, $\overline{\alpha}$ denotes the lattice direction opposite to $\alpha$. Symmetrical and anti-symmetrical components of equilibrium distribution function can also be calculated in a similar fashion as in Eq. (3). The discrete lattice velocities for the $D2Q9$ and $D3Q15$ models can be calculated as shown in Eqs. (4) and (5) [51,26]:

$$e_{\alpha,\ D2Q9}=\begin{cases}(0,0)\,, & \alpha=0\\ (\pm1,0)\,,(0,\pm1) & \alpha=1-4\\ (\pm1,\pm1)\,, & \alpha=5-8\end{cases} \quad (4)$$

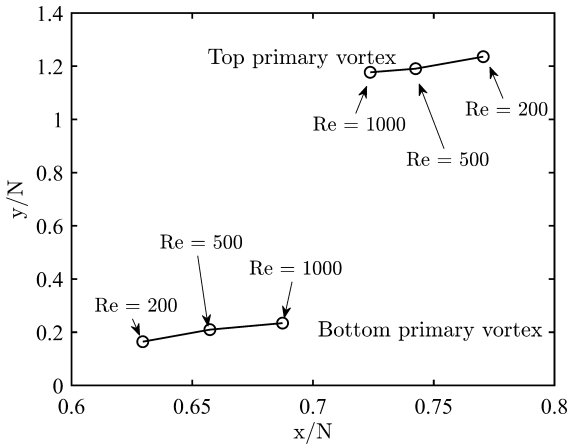


**Fig. 12.** Variation of the primary vortex with the Reynolds number at antiparallel motion in the cross shaped cavity.

$$e_{\alpha,\ D3Q15} = \begin{cases} (0,0,0) & \alpha = 0 \\ (\pm1,0,0)\,,\ (0,\pm1,0)\,,\ (0,0,\pm1) & \alpha = 1-6 \\ (\pm1,\pm1,0)\,,\ (\pm1,0,\pm1)\,,\ \ (0,\pm1,\pm1) & \alpha = 7-14. \end{cases} \tag{5}$$

The equilibrium distribution function for $D2Q9$ and $D3Q15$ models as shown in Fig. 1 can be expressed as [3]:

$$f_\alpha^{\ eq} = \rho w_\alpha \left[1 + \frac{3}{c^2}(e_\alpha \cdot u) + \frac{9}{2c^4}(e_\alpha \cdot u)^2 - \frac{3}{2c^2}(u \cdot u)\right] \tag{6}$$

where $c = {}^{\Delta x}/_{\Delta t}$ is the lattice speed, with $\Delta x$ and $\Delta t$ being the lattice spacing and time step respectively.

The lattice weights $w_\alpha$ for the $D2Q9$ and $D3Q15$ models [3] are taken as:

$$w_{\alpha,\ D2Q9} = \begin{cases} {}^4/_9\ ; & \alpha = 0 \\ {}^1/_9\ ; & \alpha = 1-4 \\ {}^1/_{36}\ ; & \alpha = 5-8 \end{cases} \tag{7}$$

$$w_{\alpha,\ D3Q15} = \begin{cases} {}^2/_9\ ; & \alpha = 0 \\ {}^1/_9\ ; & \alpha = 1-6 \\ {}^1/_{72}\ ; & \alpha = 7-14. \end{cases} \tag{8}$$

The density and velocity can be computed from the equations:

$$\rho = \sum_\alpha f_\alpha = \sum_\alpha f_\alpha^{(eq)} \tag{9}$$

$$\rho \boldsymbol{u} = \sum_\alpha f_\alpha \boldsymbol{e}_\alpha = \sum_\alpha f_\alpha^{(eq)} \boldsymbol{e}_\alpha. \tag{10}$$

Pressure can be obtained from the equation of state $p = \rho c_s^2$, where the speed of sound is taken to be $\boldsymbol{c}_s = {}^1/\sqrt{3}$. Moreover, the kinematic viscosity can be related to the symmetrical relaxation time and speed of sound as

$$\upsilon = (\tau^+ - \frac{1}{2}) c_s^2 \Delta t. \tag{11}$$

To obtain numerically stable results, the relation between the relaxation times to calculate the anti-symmetrical relaxation parameter is in accordance with the magic number relation [52]:

$$\frac{1}{4} = (\tau^+ - \frac{1}{2})(\tau^- - \frac{1}{2}). \tag{12}$$

### 2.2. Problem description

Fig. 2 depicts the geometry of the double-sided cross-shaped lid driven cavity considered in the present study. It is an extension of a square cavity to a complicated geometry, which is a symmetrized version of the staggered lid-driven cavity. This cavity comprises of two facing walls moving in the same and opposite directions with the same imposed velocity of $u$, while the other walls remain at rest. In the case of uniform wall motion, the velocities of the moving walls will be fixed to the maximum lid velocity ($U$). However, the velocities of the moving walls vary cosinusoidally according to the equation: $u = U\cos(\omega t)$ in the case of oscillating wall motions, where $t$ and $\omega$ refer to the time and oscillating frequency respectively.

In the present study, Reynolds numbers of 150, 200, 500 and 1000 are considered for the two-dimensional uniform wall motion studies, whereas Reynolds numbers of 200, 500 and 1000 have been considered for the oscillating wall motion studies. Moreover, oscillating frequencies of $2\pi/6$ and $4\pi/3$ have been considered for the cases of parallel and antiparallel wall motions.

The Reynolds number is defined as:

$$Re = \frac{UL_1}{\nu_f} \tag{13}$$

where, $L_1$ and $\nu_f$ denote the width of the cavity and kinematic viscosity of the fluid respectively. As per this geometry, the width of the cavity $L_1$ is taken to be $1.4L$ [45].

#### 2.2.1. Boundary conditions

Dirichlet boundary conditions are implemented by equating the lattice velocities at the moving walls to the fixed lid velocities. Additionally, both the velocity components at the remaining stationary walls are initialized to zero. Second order accurate bounce-back boundary conditions are also used to model the no-slip boundary across the wall [50]. Zou/He boundary conditions [53] are also applied to the moving walls when the velocity of the moving walls are known beforehand. In this case, the unknown distribution functions are computed by assuming the bounce back conditions to be valid for the non-equilibrium part of the distribution function normal to the moving wall. For the case of the top moving wall, the unknown distribution functions can be related as:

$$\begin{aligned} \rho_{tw} &= \frac{1}{(1-\upsilon_{tw})}\left(f_0 + f_1 + f_3 + 2\left(f_2 + f_5 + f_6\right)\right) \\ f_4 &= f_2 - \frac{2}{3}\rho_{tw}\upsilon_{tw} \\ f_7 &= f_5 + \frac{1}{2}(f_1 - f_3) - \frac{1}{6}\rho_{tw}\upsilon_{tw} - \frac{1}{2}\rho_{tw}u_{tw} \\ f_8 &= f_6 - \frac{1}{2}(f_1 - f_3) - \frac{1}{6}\rho_{tw}\upsilon_{tw} + \frac{1}{2}\rho_{tw}u_{tw} \end{aligned} \tag{14}$$

where $\rho_{tw}$, $u_{tw}$ and $\upsilon_{tw}$ refer to the lattice density and the velocity components at the top moving wall respectively. Similar relations can be obtained for the bottom moving wall (in the case of two-sided wall motion).

#### 2.2.2. Lattice Boltzmann method algorithm

A numerical code in MATLAB implementing LBM was developed for obtaining the relevant simulation results. A maximum lid velocity of $\boldsymbol{U} = 0.1$ was considered across the moving walls (after performing a lattice velocity independence test explained later). Initial values of the density, velocity and distribution functions at each node in the cavity were initialized to unity, zero and equilibrium distribution functions respectively, along with the initialization of the moving lid velocity with suitable boundary conditions. The developed code comprises of relevant steps present in LBM — streaming, collision, application of boundary conditions and calculation of flow variables (density and velocities) as shown in Fig. 3. Once the convergence criterion was satisfied, relevant plots like streamline profiles, vorticity contours, pressure contours and centreline velocity profiles were obtained.

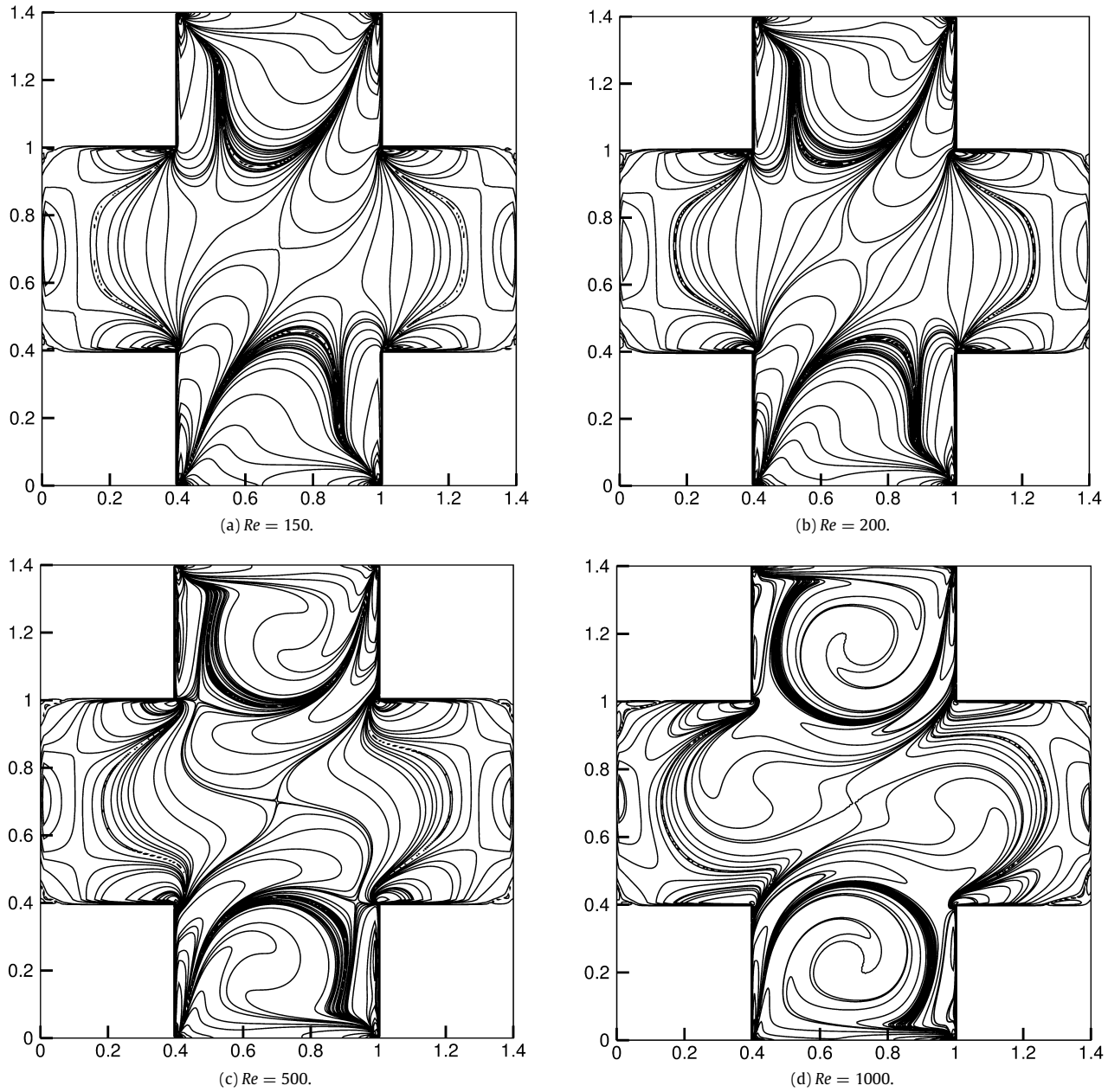


**Fig. 13.** Vorticity contours for double sided antiparallel wall uniform motion by present LBM at (a) $Re = 150$, (b) $Re = 200$, (c) $Re = 500$ and (d) $Re = 1000$.

### 2.3. Code validation study

A square lid driven cavity with single-sided wall motion was used for numerical code validation. Fig. 4(a) shows the geometry of the square cavity considered for this purpose. The streamline patterns and centreline velocity profiles were plotted at $Re = 1000$ as shown in Fig. 5. The streamline patterns at this Reynolds number depict the formation of a primary vortex at the centre of the cavity, along with two secondary vortices at the corners. Validation of the developed code was accomplished by comparing the centreline velocity profiles with Ghia et al. [19]. As observed in Fig. 6, good agreement of the results is observed, which confirms the credibility of the developed code.

Additionally, the numerical code developed for the single sided square cavity was extended to a double sided square cavity for verification. Fig. 4(b) shows the geometry of the square cavity of length $L$ with the top and bottom walls moving at a constant velocity in the opposite directions. At $Re = 400$, the streamline patterns were obtained and the centreline velocity profiles were compared with the results of Perumal and Dass [23], which were obtained using a Finite difference method (FDM). The streamline patterns in Fig. 7 reveal the formation of a primary vortex at the centre of the cavity, and good agreement of the results is observed with [23] as seen from the centreline velocity profiles shown in Fig. 8, which confirms the credibility of the developed code.

### 2.4. Convergence studies

Convergence forms a crucial step in any CFD simulation, to render physically reliable simulations. In the current study, temporal convergence and lattice convergence studies have been established to obtain satisfactory results. A modified relative $L^2$ error norm which considers the effect of both the velocity components, has been adopted to compute the residual error. The error norm is

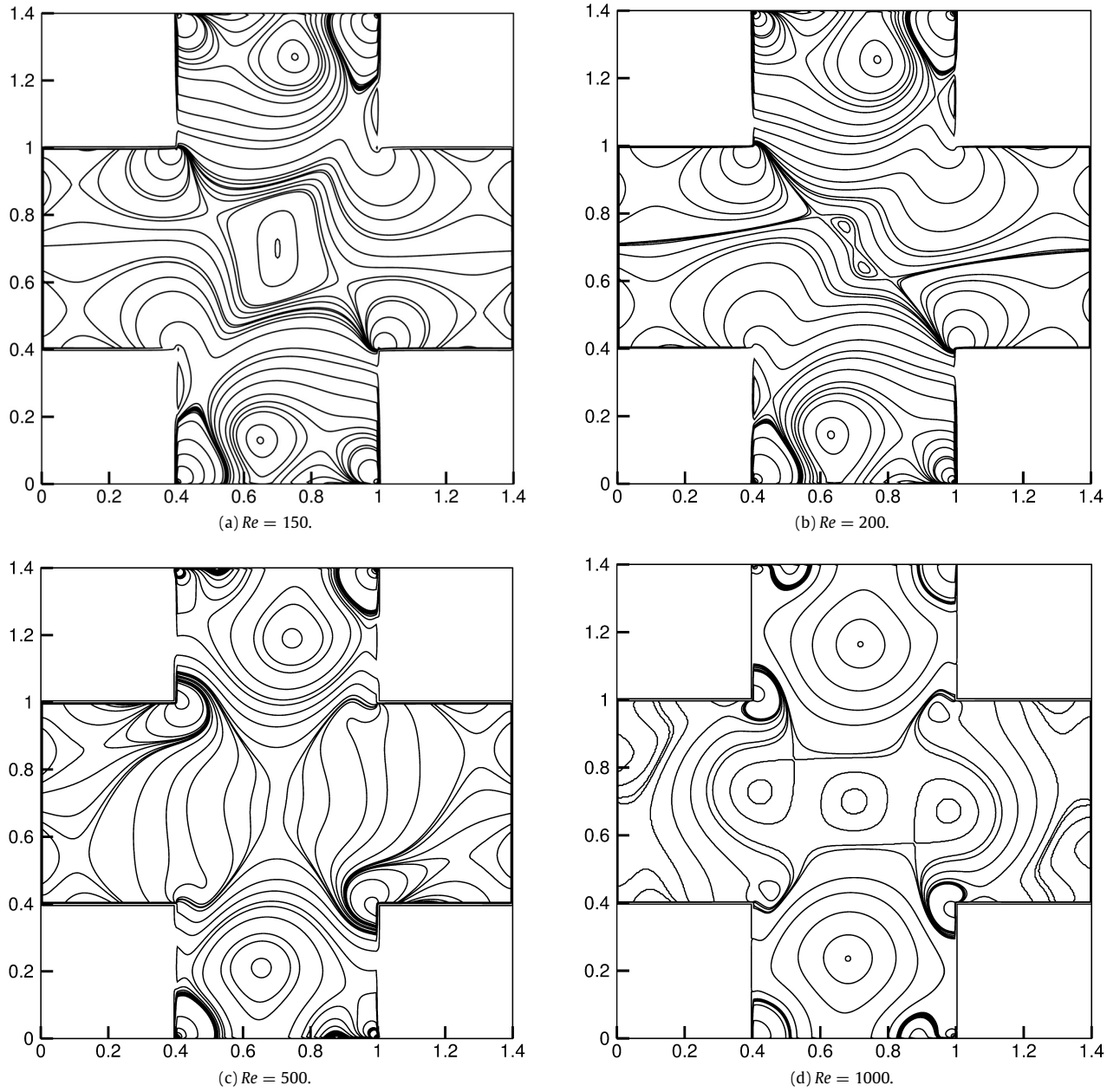


**Fig. 14.** Pressure contours for double sided antiparallel wall uniform motion by present LBM at (a) $Re = 150$, (b) $Re = 200$, (c) $Re = 500$ and (d) $Re = 1000$.

of the form:

$$Error = \sqrt{\frac{\sum_{i,j}\left(\left(u^n - u^{n-1}\right)^2 + \left(v^n - v^{n-1}\right)^2\right)}{\sum_{i,j}\left(\left(u^{n-1}\right)^2 + \left(v^{n-1}\right)^2\right)}} \tag{15}$$

where the $u^n$ and $u^{n-1}$ refer to the new and old horizontal velocity components respectively, estimated between a gap of 100 time steps. Before proceeding with the simulations in the cross shaped cavity configuration, temporal convergence studies have been performed in the antiparallel configuration of the cross shaped cavity at Reynolds numbers of 200 and 1000, as shown in Fig. 9. Steady state simulations have been subsequently obtained for all simulations till the error satisfies the convergence criterion, $Error \leq 10^{-10}$.

The main intention of plotting the history of residual errors was to identify the presence of numerical instabilities in the solution and to estimate the damping rate of the leading steady mode. At a low Reynolds number of 200, both SRT and TRT seem to induce small numerical fluctuations in the residue, and their damping rates ($-3.0756e^{-04}$ and $-3.04586e^{-04}$ respectively) are similar. However, at a high Reynolds number of 1000, the SRT approach seems to induce numerical fluctuations, while the TRT approach does not. Additionally, the initial damping rate of TRT ($-1.048e^{-04}$) is close to the one obtained by SRT ($-1.0525e^{-04}$). But, the damping rate of the TRT approach at large times decreases, and the average damping rate (a linear curve-fit) of TRT ($-6.8054e^{-05}$) comes out to be quite different from the SRT. Nevertheless, TRT seems to be a logical approach at high Reynolds numbers as its free from any numerical instabilities. Hence, in the current work, TRT model has been subsequently used for performing all numerical simulations at steady and oscillating conditions. From Fig. 9, we can further observe that SRT achieves earlier convergence than the counterpart TRT approach at $Re = 1000$, which outlines the fact that different LBM models can lead to different times for attaining convergence, and different convergence

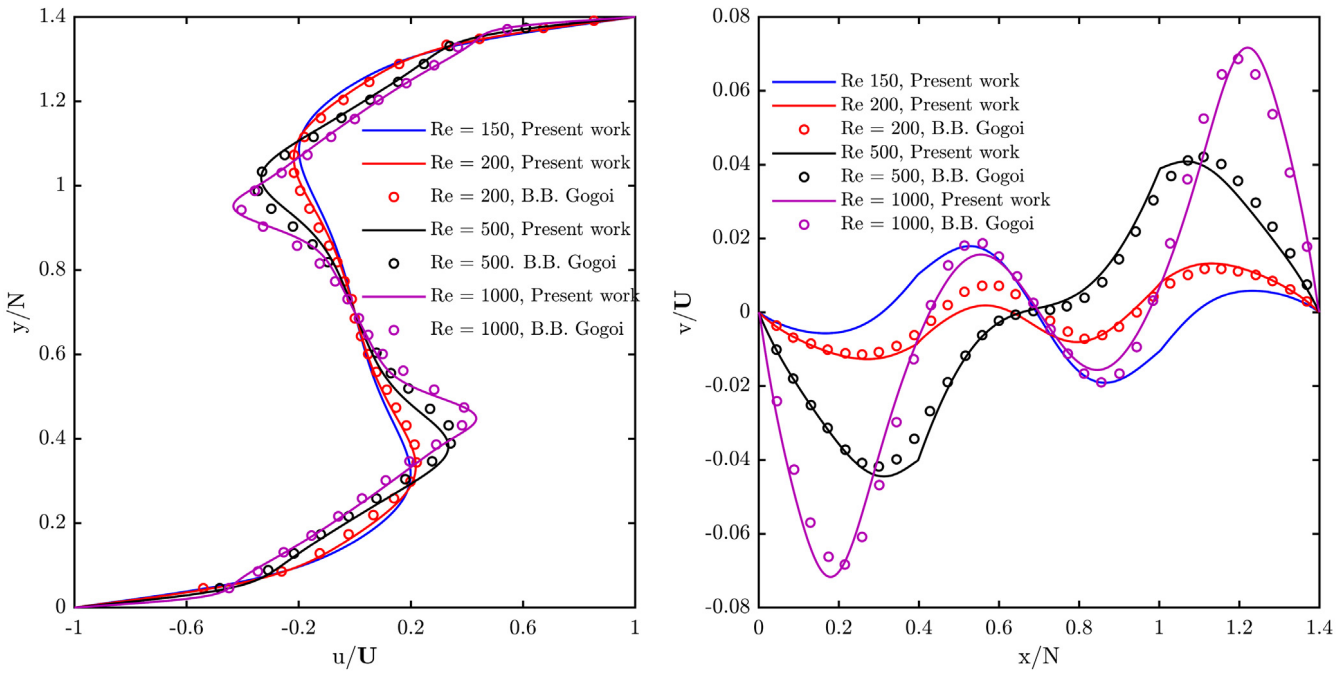


**Fig. 15.** Centreline $u$-velocity and $v$-velocity profiles for double sided antiparallel wall uniform motion by present LBM.

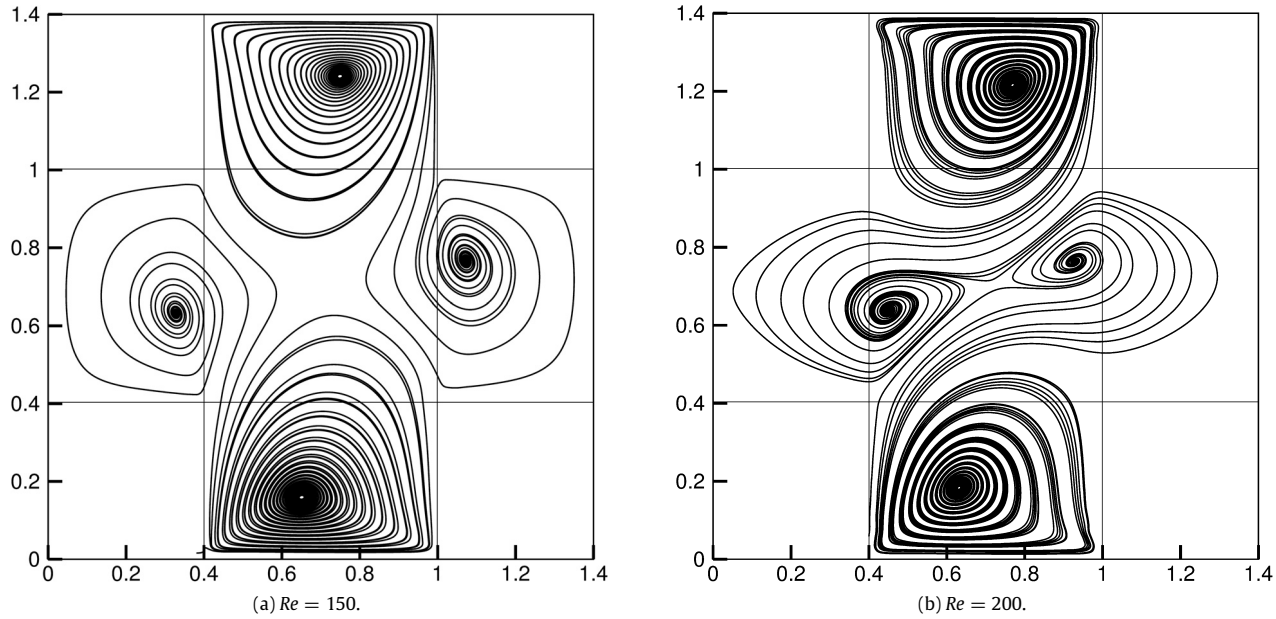

(a) $Re = 150$. (b) $Re = 200$.

**Fig. 16.** Streamline patterns for three-dimensional double sided antiparallel uniform wall motion by present LBM at (a) $Re = 150$, (b) $Re = 200$.

**Table 3**
Location of primary and secondary vortex cores for double sided antiparallel uniform wall motion.

| *Re* | Authors | Top primary vortex | | Bottom primary vortex | | Secondary vortex on the left | | Secondary vortex on the right | |
|---|---|---|---|---|---|---|---|---|---|
| | | *x* | *y* | *x* | *y* | *x* | *y* | *x* | *y* |
| 150 | Present work | 0.7657 | 1.2461 | 0.6343 | 0.1540 | 0.4311 | 0.6658 | 0.9687 | 0.7344 |
| 200 | Vicente et al. [43] | 0.7707 | 1.2326 | 0.6293 | 0.1673 | 0.5164 | 0.6778 | 0.8836 | 0.7221 |
| | Gogoi [45] | 0.7701 | 1.2300 | 0.6302 | 0.1699 | 0.4801 | 0.6660 | 0.9192 | 0.7317 |
| | Present work | 0.7705 | 1.2357 | 0.6295 | 0.1644 | 0.5309 | 0.6790 | 0.8691 | 0.7212 |
| 500 | Vicente et al. [43] | 0.7431 | 1.1876 | 0.6569 | 0.2122 | 0.7000 | 0.7000 | – | – |
| | Gogoi [45] | 0.7400 | 1.1800 | 0.6600 | 0.2200 | 0.7000 | 0.7000 | – | – |
| | Present work | 0.7425 | 1.1906 | 0.6573 | 0.2097 | 0.7000 | 0.7001 | – | – |
| 1000 | Vicente et al. [43] | 0.7255 | 1.1721 | 0.6745 | 0.2278 | 0.4701 | 0.7322 | 0.9299 | 0.6776 |
| | Gogoi [45] | 0.7229 | 0.1684 | 0.6800 | 0.2369 | 0.4700 | 0.7399 | 0.9600 | 0.6600 |
| | Present work | 0.7237 | 1.1770 | 0.6874 | 0.2343 | 0.4428 | 0.7294 | 0.9684 | 0.6819 |

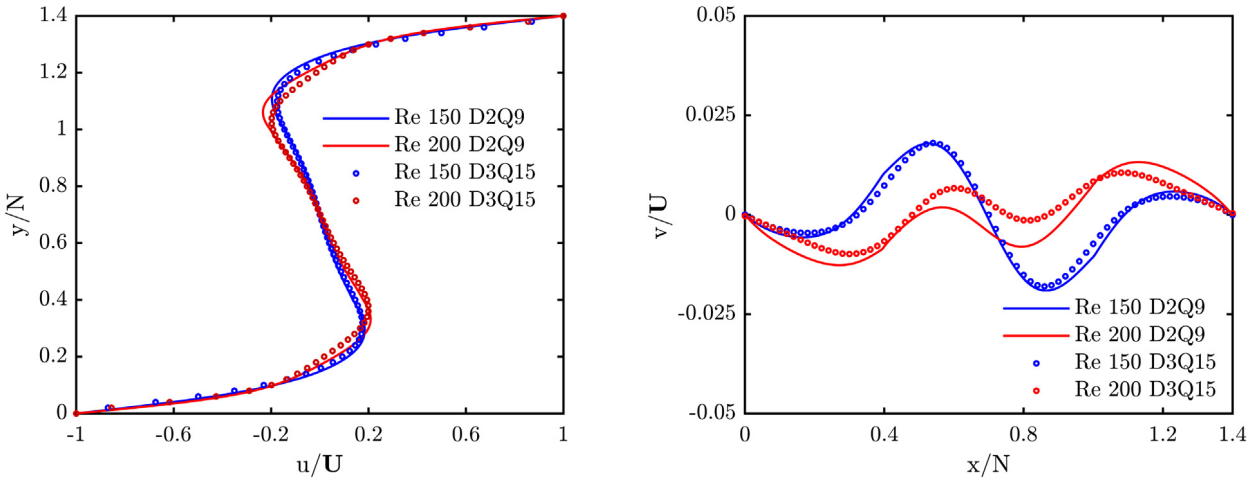


(a) $u$-velocity profile. (b) $v$-velocity profile.

**Fig. 17.** Centreline (a) $u$-velocity and (b) $v$-velocity profiles for three-dimensional double sided antiparallel uniform wall motion by present LBM.

**Table 4**
Location of primary and secondary vortex cores for double sided parallel uniform wall motion.

| *Re* | Left top secondary vortex | | Left bottom secondary vortex | | Right top secondary vortex | | Right bottom secondary vortex | | Bottom primary vortex | | Top primary vortex | |
|---|---|---|---|---|---|---|---|---|---|---|---|---|
| | *x* | *y* | *x* | *y* | *x* | *y* | *x* | *y* | *x* | *y* | *x* | *y* |
| | Present work | | | | | | | | | | | |
| 150 | 0.2705 | 0.8601 | 0.2706 | 0.5399 | 1.0466 | 0.8504 | 1.0466 | 0.5497 | 0.7547 | 0.1478 | 0.7548 | 1.2522 |
| 200 | 0.2675 | 0.8625 | 0.2675 | 0.5375 | 1.0275 | 0.8475 | 1.0275 | 0.5525 | 0.7625 | 0.1535 | 0.7625 | 1.2475 |
| 500 | 0.3175 | 0.8425 | 0.3175 | 0.5571 | 0.9302 | 0.8337 | 0.9302 | 0.5664 | 0.7554 | 0.2052 | 0.7554 | 1.1948 |
| 1000 | 0.4566 | 0.8266 | 0.4566 | 0.5735 | 0.8632 | 0.8185 | 0.8632 | 0.5816 | 0.7295 | 0.2303 | 0.7294 | 1.1698 |
| | Gogoi [45] | | | | | | | | | | | |
| 200 | 0.2200 | 0.8600 | 0.2100 | 0.5300 | 1.00 | 0.8400 | 1.01 | 0.5500 | 0.77 | 0.1700 | 0.77 | 1.2300 |
| 500 | 0.3100 | 0.8300 | 0.3200 | 0.5600 | 0.93 | 0.8300 | 0.92 | 0.5800 | 0.74 | 0.2400 | 0.74 | 1.1600 |
| 1000 | 0.3900 | 0.8500 | 0.4000 | 0.5600 | 0.89 | 0.8100 | 0.89 | 0.5900 | 0.72 | 0.2500 | 0.72 | 1.1500 |

rates. These observations are consistent with the studies initially performed by Perez et al. [54], who compared MRT and SRT models.

On the other hand, lattice convergence tests were performed for three different lattice sizes ranging from 176 × 176, 281 × 281 and 561 × 561 in the double sided cross cavity at antiparallel configuration. As observed in Table 1, not much improvement in the vortex positions is observed on increasing the lattice size from 281 × 281 to 561 × 561. Hence, an optimum lattice size of 281 × 281 was selected, as the lattice size of 561 × 561 would consume enormous computational resources.

### 2.5. Lattice velocity independence study

In LBM, any suitable velocity which satisfies the incompressible flow regime can be adopted for the simulations. However, the number of time steps required for convergence decreases as the lattice velocity increases. Thus, with a motive of utilizing less computational resources, an optimum lattice velocity of 0.1 which does not cause any significant change in the results was chosen. This was accomplished by comparing the maximum and minimum velocity components obtained (as seen in Table 2) for lid velocities of 0.05 and 0.1, at $Re = 1000$ in the cross-shaped cavity with antiparallel wall motion.

## 3. Results and discussions

In order to study the performance of the present LBM model, it is applied to four pertinent fluid flow problems. These include (i) cross shaped cavity with antiparallel uniform wall motion (ii) cross shaped cavity with parallel uniform wall motion (iii) cross shaped cavity with antiparallel oscillating wall motion and (iv) cross shaped cavity with parallel oscillating wall motion.

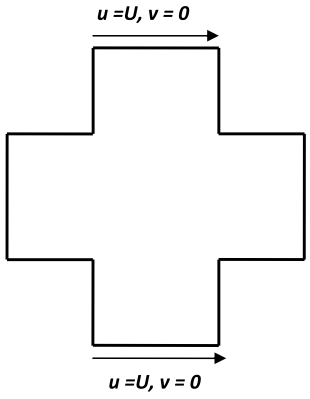


**Fig. 18.** Schematic representation of double sided cross shaped cavity with parallel uniform wall motion.

### 3.1. Cross shaped cavity with antiparallel uniform wall motion

Fig. 10 shows the schematic representation of double sided cross shaped cavity with antiparallel uniform wall motion. In this case, the top and bottom walls move in the opposite directions with equal fixed velocities, while the other walls remain at rest.

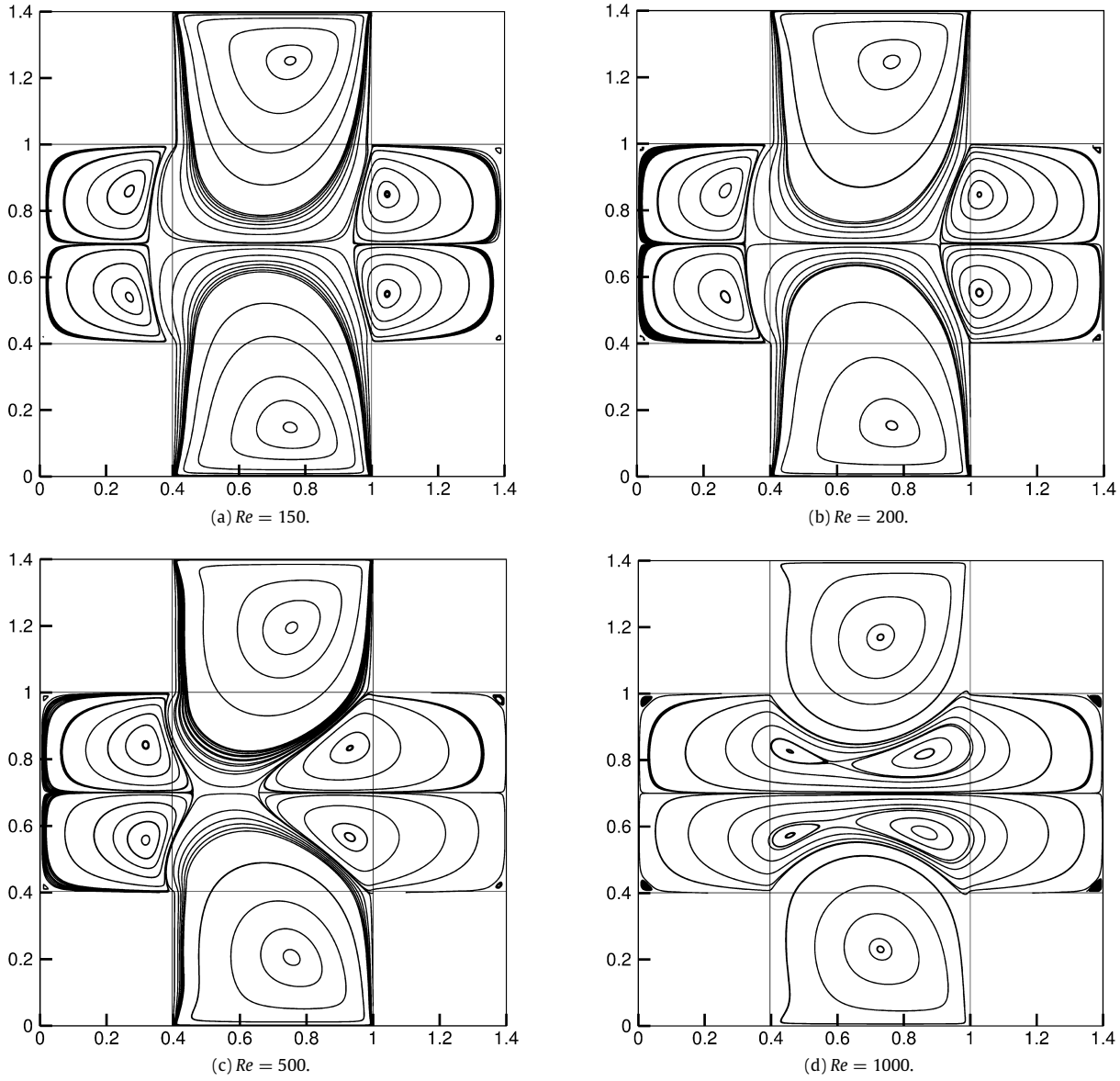


**Fig. 19.** Streamline patterns for double sided cross shaped parallel wall uniform motion by present LBM at (a) $Re = 150$, (b) $Re = 200$, (c) $Re = 500$ and (d) $Re = 1000$.

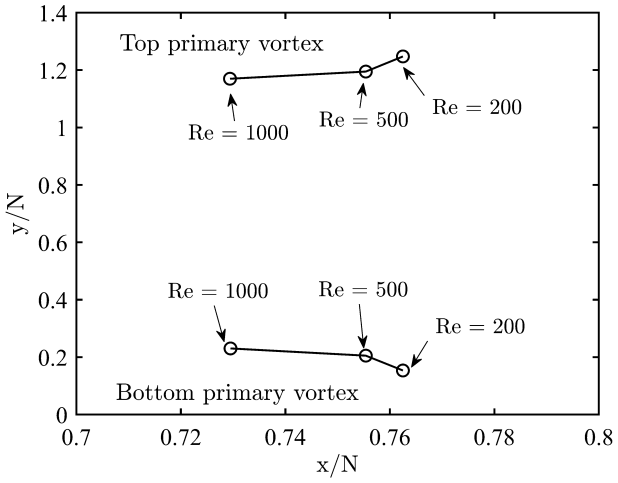


**Fig. 20.** Variation of the primary vortex with the Reynolds number at parallel motion in the cross shaped cavity.

As depicted in each streamline pattern, the moving walls induce primary vortices in its immediate vicinity. Moreover, the streamlines in this case are found to be skew-symmetric with respect to the centre of the cavity.

Fig. 11 shows the streamline patterns obtained for $Re = 150$, 200, 500 and 1000. From Fig. 11(a), two primary vortices are seen on the top and bottom portions of the cavity. Additionally, two secondary vortices are also observed opposite to each other on the left and right sides of the cavity in a skew-symmetrical fashion (termed as the two eddy pattern analogous to the case in the staggered cavity [46]) at $Re = 150$. As the Reynolds number increases to 200 (Fig. 11(b)), two other secondary recirculation regions with opposite sense of rotation appear to move closer towards the centre of the cavity domain. This type of flow pattern is termed as the cat's eyes flow pattern. Increasing the Reynolds number to $Re = 500$ (Fig. 11(c)) results in the merging of secondary vortices to form an elliptical shaped vortex (termed as the merged vortex state) at the centre of the cavity domain. Interestingly, the formation of this merged vortex state is also seen in the case of staggered lid driven cavity [46]. At high $Re = 1000$ (Fig. 11(d)), the

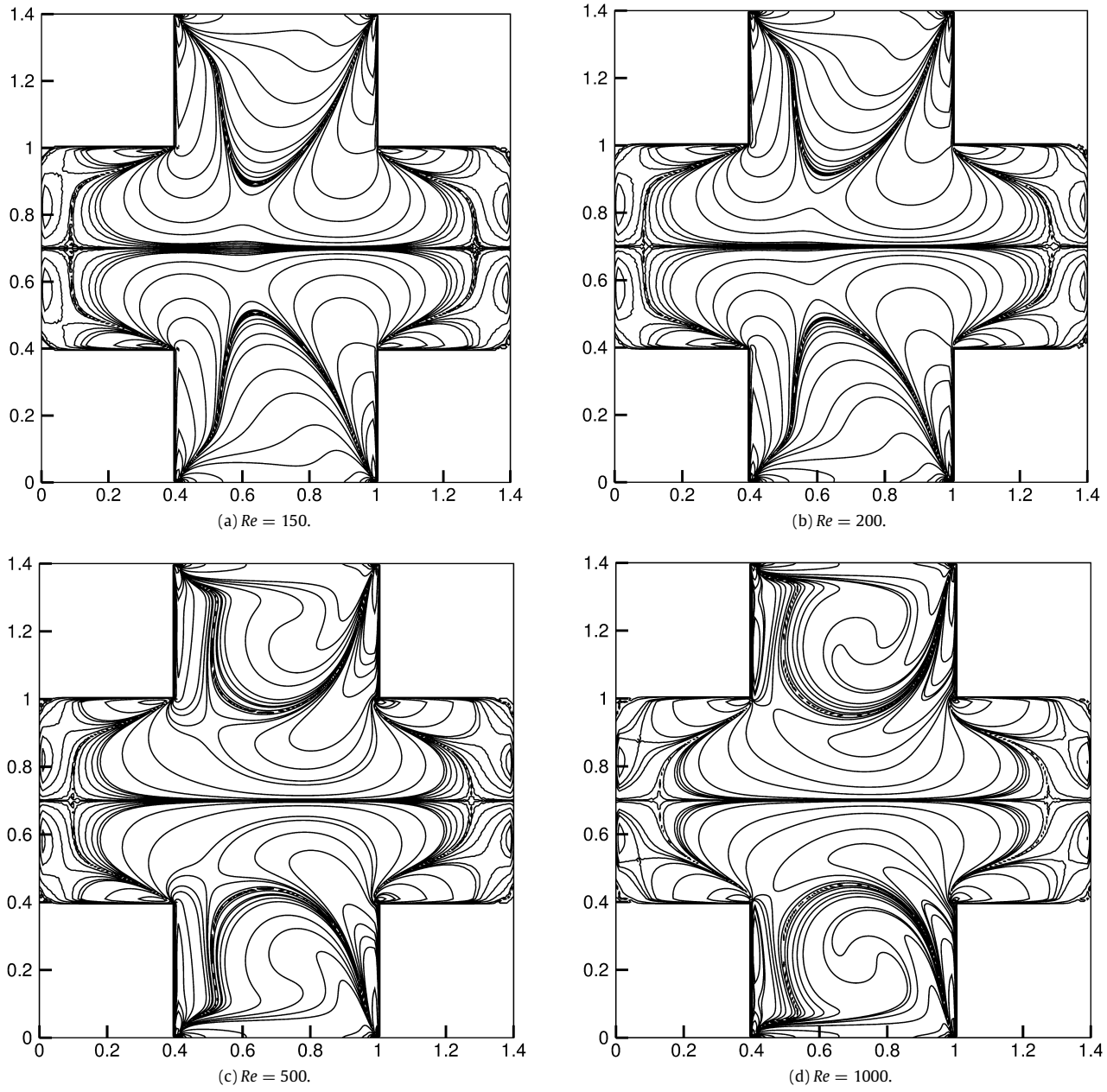


**Fig. 21.** Vorticity contours for double sided parallel wall uniform motion at (a) $Re = 150$, (b) $Re = 200$, (c) $Re = 500$ and (d) $Re = 1000$.

secondary vortices formed at $Re = 500$ tend to get separated to form cat's eyes flow patterns again. This characteristic appearance and disappearance of the cat's eyes flow patterns with the change in Reynolds numbers is also verified by Gogoi [45]. It is also witnessed that as the Reynolds number increases, the top and bottom primary vortex cores tend to move away from the top and bottom walls of the cavity, towards the vertical centreline of the cavity along with a shift in the secondary vortex position towards the principal cavity centre (as seen in Fig. 11 for the case of $Re = 500$ and in Fig. 12). A similar movement of the primary vortex towards the cavity centre has been fundamentally observed in a single-sided cavity [19], and in the staggered cavity as well [46].

A stark difference which distinguishes the flow behaviour between the staggered and cross-shaped cavity configurations is demonstrated at Reynolds numbers between 400–1000. In that case, the flow behaviour in the staggered configuration remains as the merged vortex state, with no signs of any change. Whereas, in the cross-shaped configuration, the flow transforms into the two eddy pattern with the formation of a merged vortex state at an intermediate Reynolds number.

The present LBM streamline patterns of $Re = 200$, 500 and 1000 are in excellent agreement with Vicente et al. [43] and Gogoi and Kalita [44,45]. Additionally, tertiary corner vortices have been suitably captured for each streamline pattern in the cross shaped cavity, which were not previously reported by Vicente et al. [43]. The vorticity contours of antiparallel uniform wall motion are also depicted in Fig. 13. Results show that the moving wall generates vorticity which diffuses inside the cavity, and this diffusion acts as the driving mechanism of the flow. One can also observe the formation of strong vorticity gradients at the walls (moving and stationary) situated in the top and bottom portions of the cavity domain, with an increase in the Reynolds number. At high Reynolds numbers, the primary vortex cores have almost no viscous motion (visible through the absence of gradients close at the primary

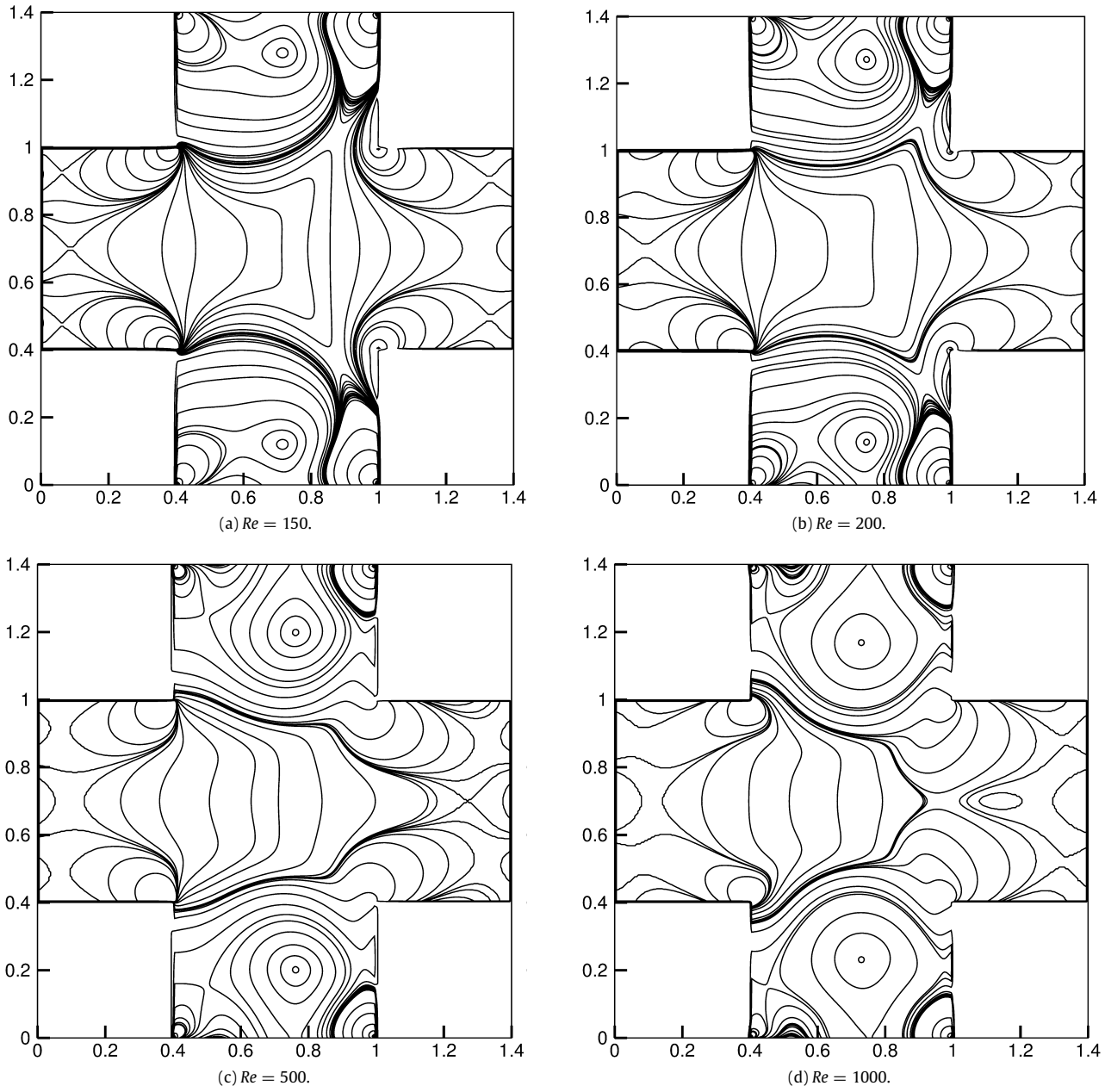


**Fig. 22.** Pressure contours for double sided parallel wall uniform motion at (a) $Re = 150$, (b) $Re = 200$, (c) $Re = 500$ and (d) $Re = 1000$.

vortex centres). This unique motion can be typically observed in the flow associated with lid driven cavities [4], and is also observed in the parallel wall motion of the cross shaped cavities. However, the effect of these gradients seem to diminish at the walls present in the left and right portions of the cavity domain. Additionally, a star-shaped structure can be seen in the vorticity contours, which seems to rotate about the cavity centre at high Reynolds numbers of 500 and 1000. Again, these vorticity contours at $Re = 200$, 500 and 1000 of present LBM results exhibit an excellent match with the published results [43–45]. Fig. 14 presents the pressure contours obtained directly using the equation of state for $Re = 150$, 200, 500 and 1000. The centreline velocity profiles are listed in Fig. 15. Good agreement of the velocity profiles with Gogoi [45] can be observed, which confirms the reliability of the current mesoscopic approach. Similar to the variation of the velocity profiles in the staggered cavity [46], stronger velocity gradients can be observed near the walls in the case of the cross-shaped cavity too, as the inertial forces increase with the Reynolds number.

Table 3 presents the locations of the vortices obtained by using LBM for $Re = 150$, 200, 500 and 1000. All these results are in good agreement with Vicente et al. [43] and Gogoi [45], which further substantiates the accuracy of the present LBM computations. From the results predicted above, it can be concluded that the flow behaves differently as the Reynolds number is varied from 150 to 1000, which is greatly affected by the flow pattern and shape of the geometry. The presented results thus demonstrate the capability of the mesoscopic LBM method in predicting complex fluid flow behaviour in the double sided cross-shaped cavity problem. The cross-shaped antiparallel uniform wall motion results thus provide us confidence to apply the present LBM to investigate other types of complex fluid flow motions.

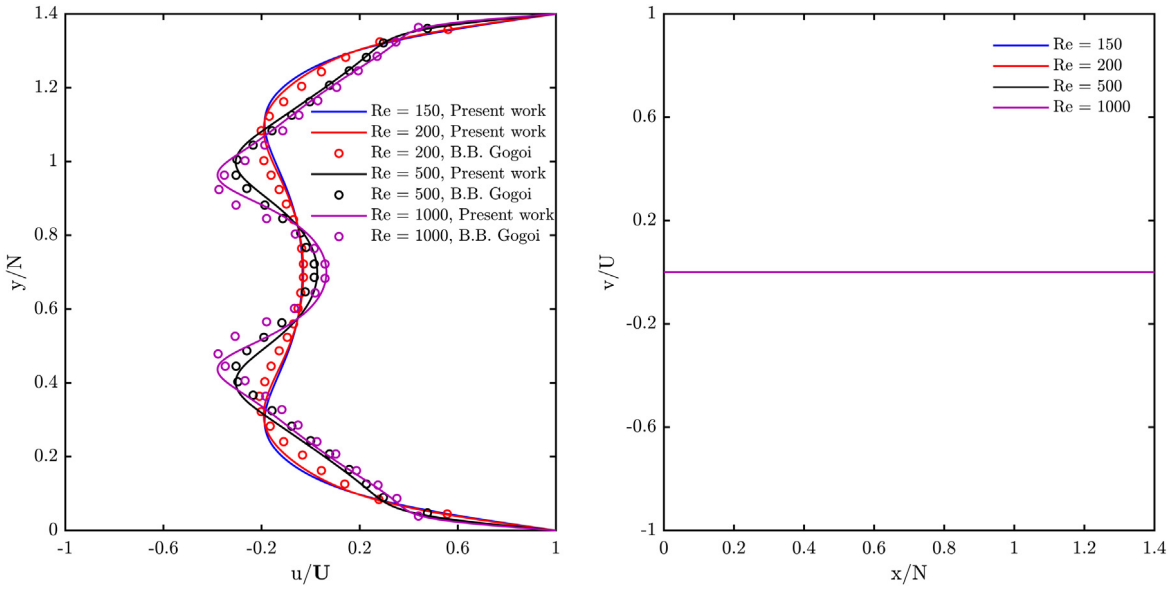


**Fig. 23.** Centreline $u$-velocity and $v$-velocity profiles for double sided parallel wall uniform motion.

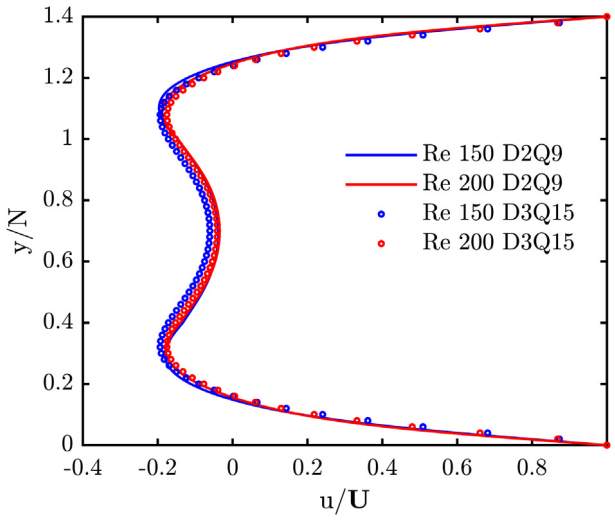


**Fig. 24.** Centreline $u$-velocity profile for three-dimensional double sided parallel wall uniform motion by present LBM.

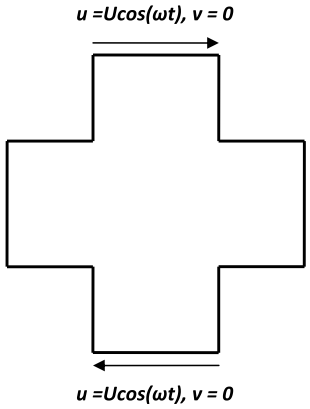


**Fig. 25.** Schematic representation of double sided cross shaped cavity with antiparallel oscillating wall motion.

### 3.1.1. Three dimensional boundary layer effect

To study the three-dimensional boundary layer effect, $D3Q15$ lattice model is used in the present work. Fig. 16(a) and (b) shows the stream traces in the $x-y$ plane sliced at the mid-span ($z = 0.5$) of the cavity for $Re = 150$ and 200. The $D3Q15$ model consumes less memory and computational time compared with $D3Q19$ and $D3Q27$ models, which motivated us to apply it to this geometry. Fig. 16(a) clearly shows the primary and secondary vortices which resemble the two-dimensional streamline pattern obtained previously for $Re = 150$; However at $Re = 200$ (Fig. 16(b)), the cat's eyes flow pattern has not been fully developed unlike the case in a two-dimensional cavity. Owing to the boundary layer effect of the stationary walls, the mid-span ($z = 0.5$) flow in the 3-D cross-shaped cavity is slightly different from that in the 2-D cross-shaped cavity case. However, at low $Re$, the 3-D cavity flow patterns in the symmetry plane are similar to those of a 2-D cavity case. The present computations are carried out on a modest $71 \times 71 \times 51$ lattice size.

Fig. 17(a) and (b) shows the variations of $u$-velocity and $v$-velocity along the vertical and horizontal centrelines along the mid-span ($z = 0.5$) at $Re = 150$ and 200. As the Reynolds number increases, an increase in the discrepancy between the two and three-dimensional velocity profiles (at mid-plane) is noticed. The present 3D mid-span velocity profiles plotted alongside corresponding 2D profiles reveal the fact that as Reynolds number increases the influence of the boundary layer effects due to walls also increases.

### 3.2. Cross shaped cavity with parallel uniform wall motion

In this case as shown in Fig. 18, the top and bottom walls move in the same direction with equal fixed velocities. In contrast to the anti-parallel wall motion, the streamlines in this case are found to be symmetrical with respect to the centreline horizontal axis. The parallel flow configuration of the geometry has been chosen for this present work due to the gradual development of a free-shear layer at the centre of the cavity domain, in addition to the formation of secondary vortices and other exciting flow features.

Fig. 19 shows the streamline patterns obtained for $Re = 150$, 200, 500 and 1000 using the TRT model. At low Reynolds numbers

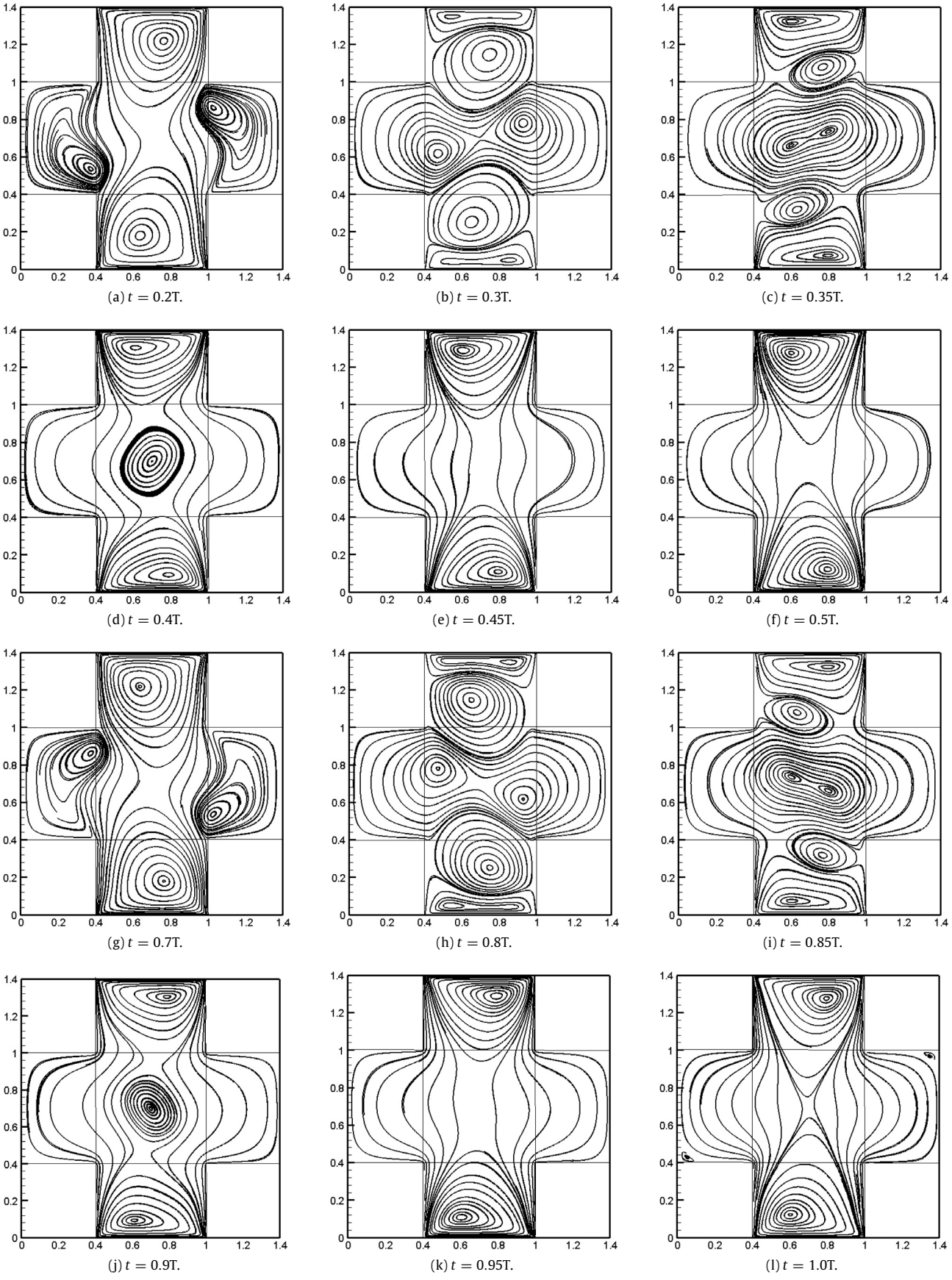

(a) $t = 0.2$T. (b) $t = 0.3$T. (c) $t = 0.35$T.

(d) $t = 0.4$T. (e) $t = 0.45$T. (f) $t = 0.5$T.

(g) $t = 0.7$T. (h) $t = 0.8$T. (i) $t = 0.85$T.

(j) $t = 0.9$T. (k) $t = 0.95$T. (l) $t = 1.0$T.

**Fig. 26.** Streamline plots during the cycle for double sided antiparallel oscillating wall motion at $Re = 200$, $\omega = 2\pi/6$.

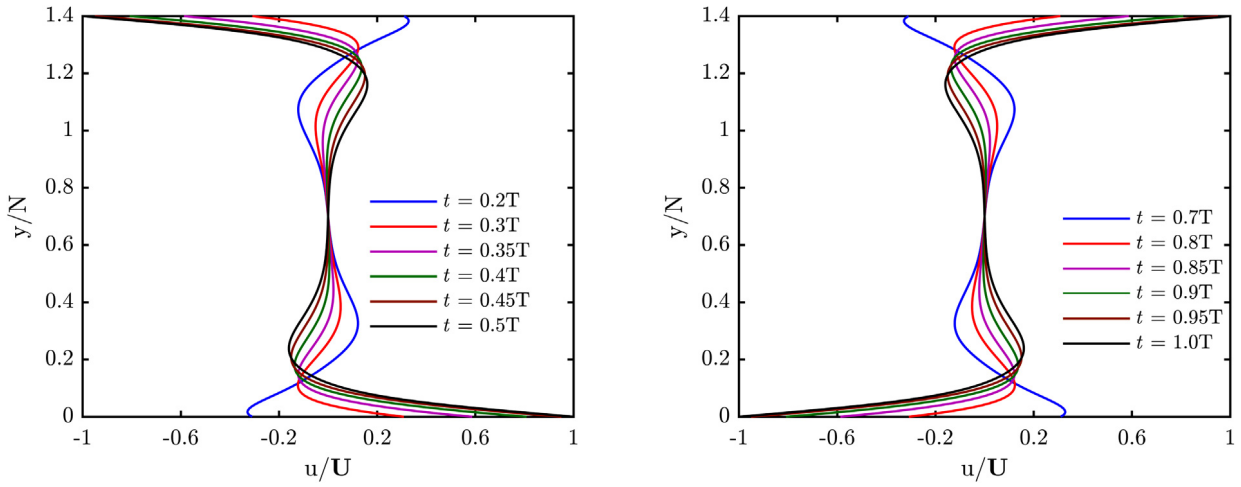


(a) First half of the cycle. (b) Second half of the cycle.

**Fig. 27.** Centreline $u$-velocity profiles for double sided antiparallel oscillating wall motion during (a) First half of the cycle and (b) Second half of the cycle.

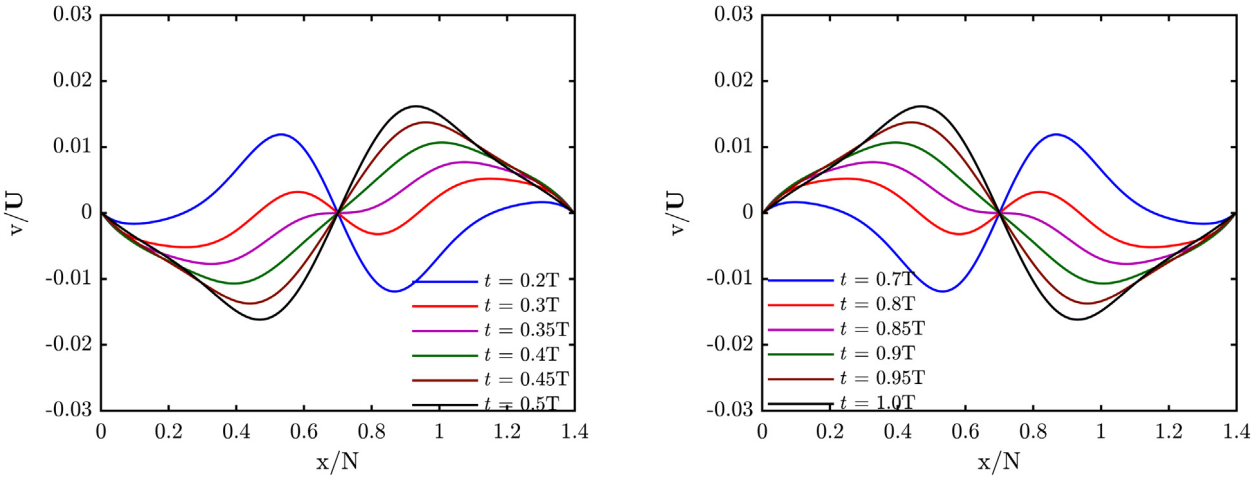


(a) First half of the cycle. (b) Second half of the cycle.

**Fig. 28.** Centreline $v$-velocity profiles for double sided antiparallel oscillating wall motion during (a) First half of the cycle and (b) Second half of the cycle.

of $Re = 150$ and 200 (Fig. 19(a)), a pair of symmetric counter-rotating secondary vortices are formed on the left and the right halves of the cavity, along with a pair of primary vortices close to the moving walls. In contrast to the anti-parallel uniform wall motion, the secondary vortices formed in the central portion of the cavity are separated by a shear layer, similar to the case of a double sided square cavity in parallel wall motion [23,55]. Contrast to this case, the shear layer in the case of staggered cavity [49] forms along the shorter diagonal, as the top and bottom portions of the cavity are offset by a certain distance. Additionally, the formation of a single secondary vortex closer to the right wall in turn destroys the symmetricity of the streamline patterns in the staggered case, though its symmetric in the cross-shaped cavity. As the Reynolds number increases to 500 (Fig. 19(c)), the cores of the two secondary vortices on the right half of the cavity tend to move closer towards the centre of the cavity. However, there is a restriction on their size due to the bounding walls and viscous shear layer between them. As the Reynolds number is further increased to 1000 (Fig. 19(d)), it is observed that the vortex cores on the left half of the cavity also tend to move closer towards the centre of the cavity, resulting in the formation of cat's eyes flow pattern. This result is expected on account of the symmetric nature of the geometry and boundary conditions in the cross-shaped cavity. For precise computations, tertiary corner vortices have been again suitably captured in this case of parallel motion too. From Fig. 20, the movement of the primary vortices towards the vertical centreline of the cavity, on increasing the Reynolds number can be observed.

The vorticity and pressure contours of this geometry are depicted in Figs. 21(a)–(d) and 22(a)–(d) respectively. In Fig. 23(a)–(b), the centreline velocity profiles are validated with the previous results by Gogoi [45]. The centreline $v$-velocity profile shows the value close to zero. This behaviour can be attributed to the presence of shear layer, where both the velocity components turn zero. The pressure contours, vorticity contours and centreline velocity profiles are symmetrical analogous to the streamline profiles. Additionally, Table 4 provides the locations of the vortices obtained by the present study for $Re = 150$, 200, 500 and 1000 making

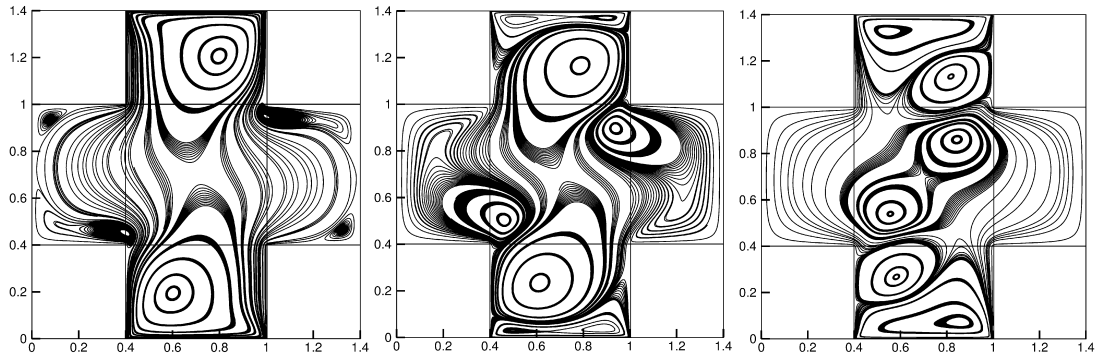

(a) $Re = 500$.

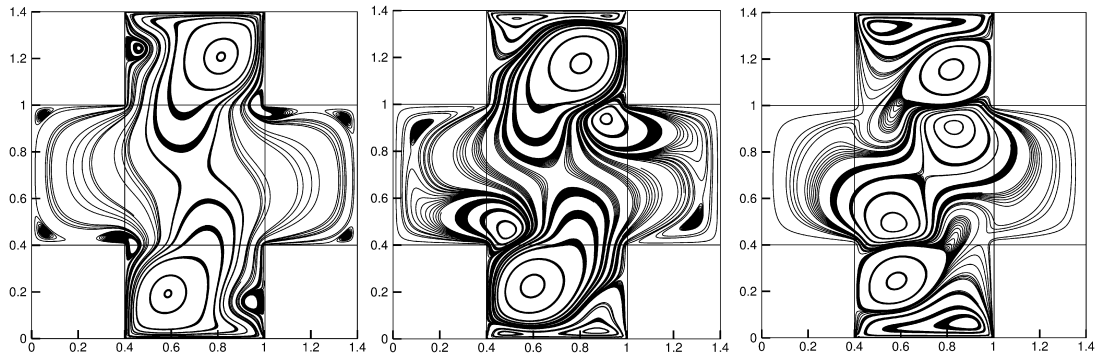

(b) $Re = 1000$.

**Fig. 29.** Streamline plots for double sided antiparallel oscillating wall motion at $t = 0.2$T (left), $t = 0.3$T (centre) and $t = 0.4$T (right) for various Reynolds numbers at $\omega = 2\pi/6$.

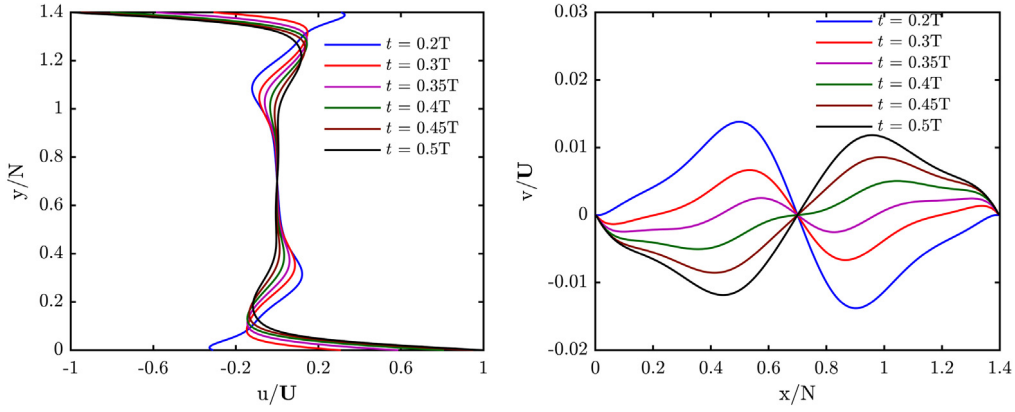


(a) $Re = 500$.

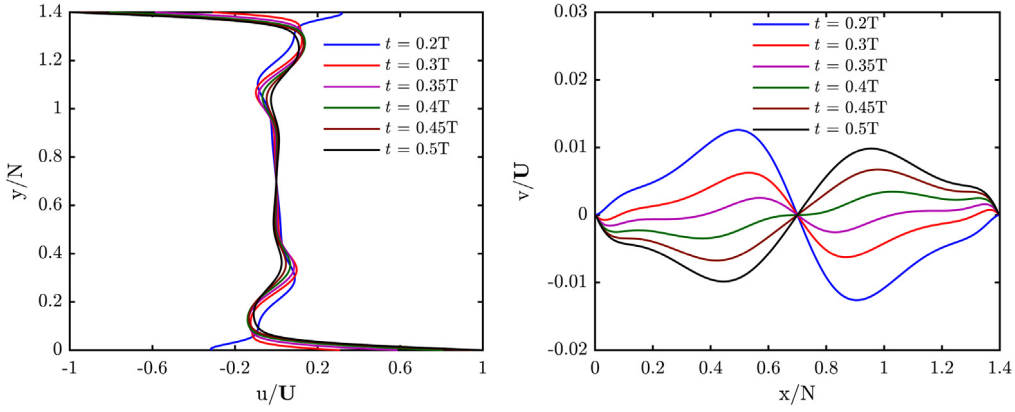


(b) $Re = 1000$.

**Fig. 30.** Centreline velocity profiles for double sided antiparallel oscillating wall motion during the first half of the cycle for various Reynolds numbers at $\omega = 2\pi/6$.

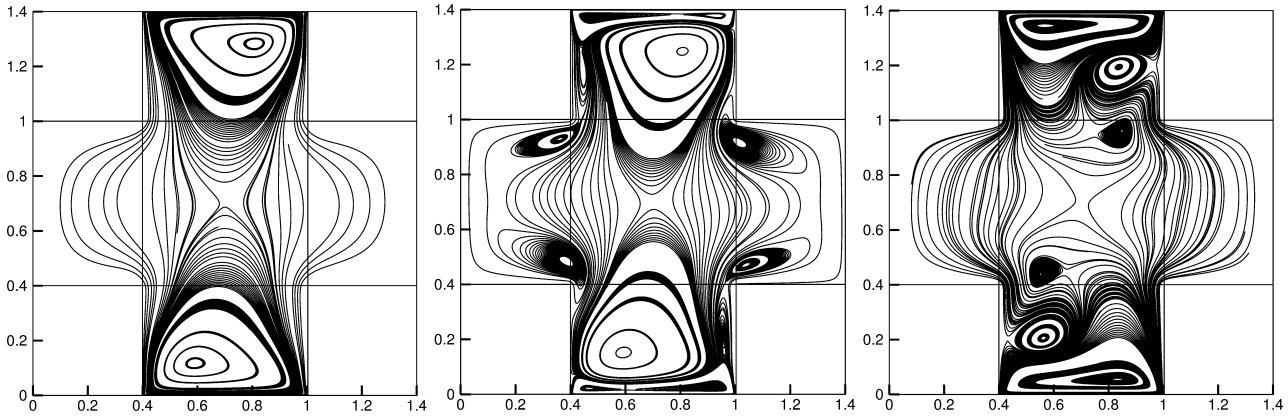

(a) $Re = 200$.

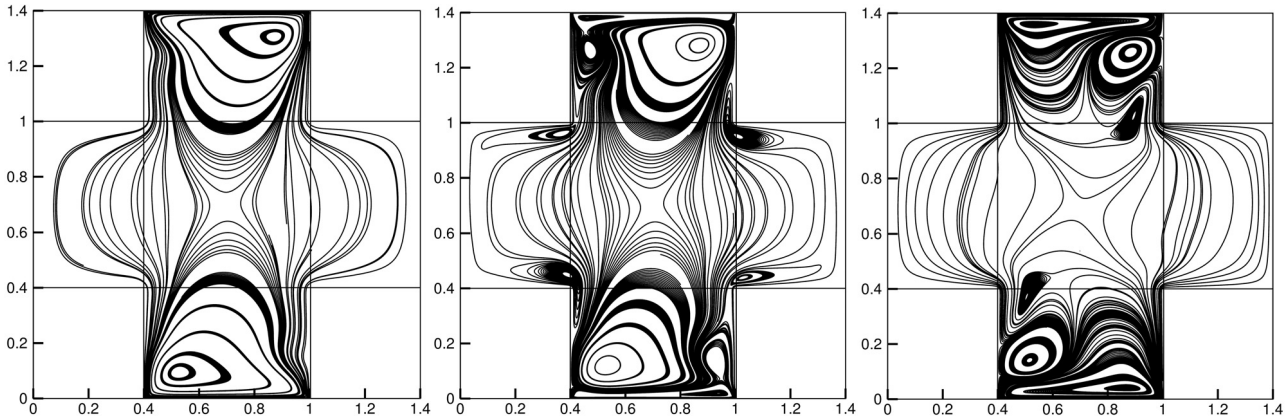

(b) $Re = 500$.

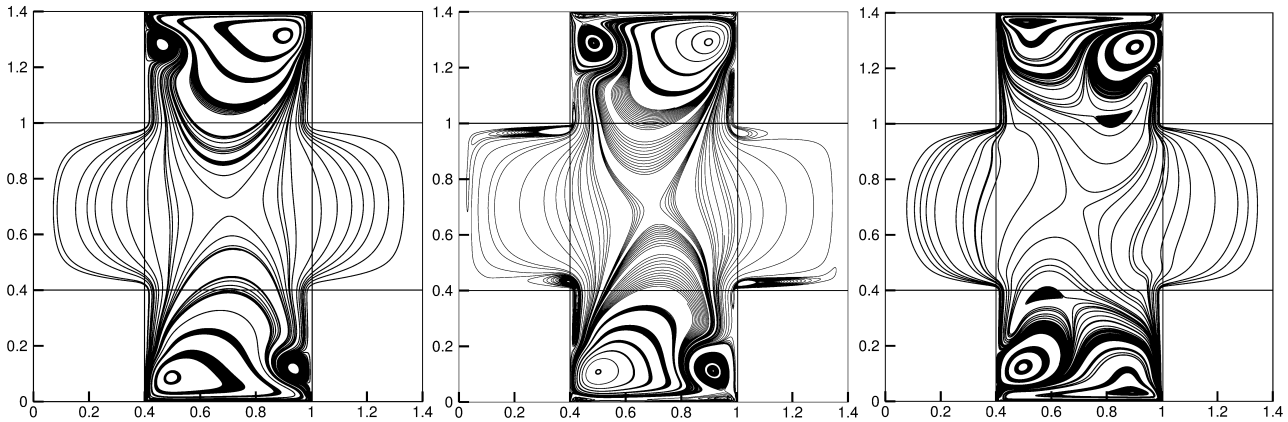

(c) $Re = 1000$.

**Fig. 31.** Streamline plots for double sided antiparallel oscillating wall motion at $t = 0.2$T (left), $t = 0.3$T (centre) and $t = 0.4$T (right) for various Reynolds numbers at $\omega = 4\pi/3$.

it easier for the future researchers to compare their results. Further, the vortex locations are in close agreement with Gogoi [45], which again confirms the validity of the current mesoscopic approach.

To study the three-dimensional boundary layer effect, centreline $u$-velocity profiles are plotted at $Re = 150$ and 200 using the D3Q15 model. Fig. 24 shows the variation of $u$-velocity along the horizontal centreline on the$z = 0.5$ plane. It is seen that the difference in velocity profiles of 2D and 3D are insignificant in both the cases of Reynolds number. Similar trends have also been observed by Perumal [56] for low Reynolds number in 3-D double sided cavity.

### 3.3. Cross shaped cavity with antiparallel oscillating wall motion

In this subsection, the flow behaviour in a cross-shaped cavity with antiparallel oscillating wall motion for varying Reynolds numbers and frequencies is studied using the TRT model of LBM. Extensive review of literature reveals that very few studies have been carried out pertaining to the oscillating wall motion, and none concerning cross shaped cavities. Fig. 25 depicts the geometry and boundary conditions for antiparallel oscillating wall motion.

The streamline plots at various time instants have been initially captured at $Re = 200$ and oscillating frequency of $\omega = 2\pi/6$ as seen in Fig. 26. The streamline plots have been divided into two half

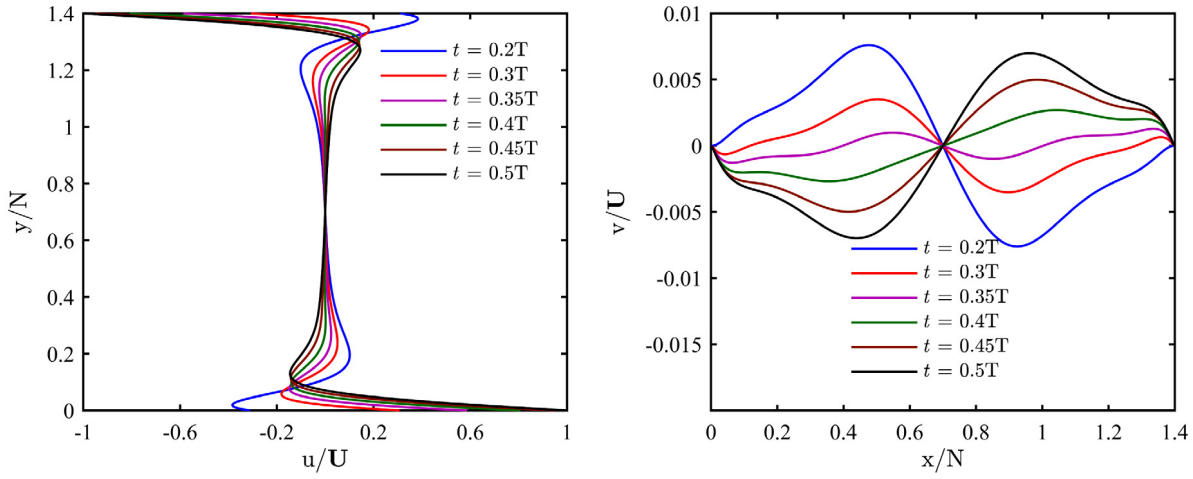


(a) *Re* = 200.

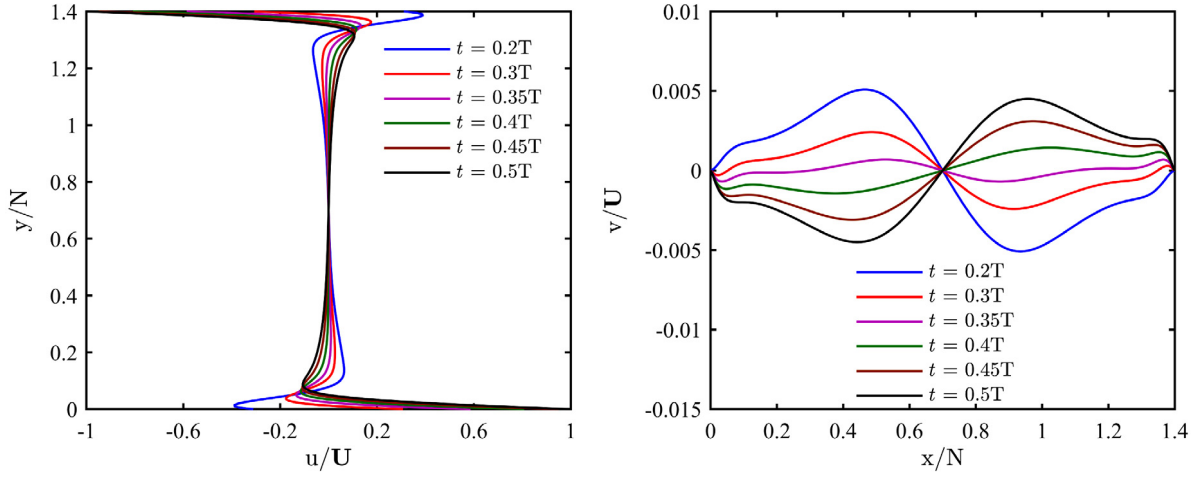


(b) *Re* = 500.

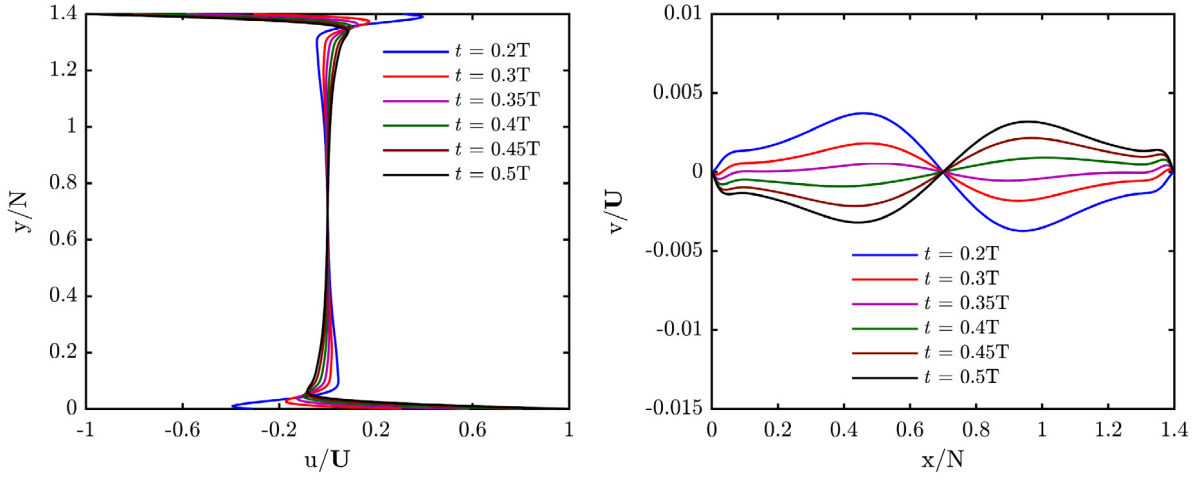


(c) *Re* = 1000.

**Fig. 32.** Centreline velocity profiles for double sided antiparallel oscillating wall motion during the first half of the cycle for various Reynolds numbers at $\omega = 4\pi/3$.

cycles, with the streamline plots in both the halves being mirror images of each other due to the reversal of the wall velocity directions. The streamlines at each time instant are skew-symmetric along the cavity centre, similar to the case of antiparallel uniform wall motion.

Initially (at $t = 0.2$T), a pair of primary vortices generated due to the motion of the lids can be observed at the top and bottom halves of the cavity, along with a pair of secondary vortices close to the left and right halves of the domain. At a later time instant (0.3T), the secondary vortices tend to get merged towards the

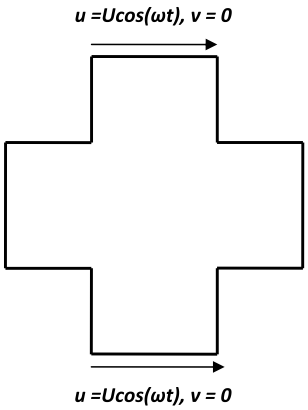


**Fig. 33.** Schematic representation of double sided cross-shaped cavity with parallel oscillating wall motion.

cavity centre, which have a striking similarity with the streamline patterns found in the case of uniform antiparallel wall motion (Fig. 11(b)). However, the shear motion of the fluid layer between the primary vortices and moving lids causes the formation of another tertiary vortex. This tertiary vortex grows as time progresses (at $t = 0.35$T), with subsequent shrinkage of the primary vortices and fusion of the secondary vortices ($t = 0.4$T). At the end of the first half cycle ($t = 0.45$T and 0.5T), the primary vortices dominate the entire fluid domain. See Fig. 26.

The centreline $u$ and $v$ velocity profiles are depicted in Figs. 27(a)–(b) and 28(a)–(b) respectively. A stark difference between the oscillating and uniform case with respect to the velocity variation, lies in the complex alternation of local fluid velocities. For instance, in the case of uniform antiparallel wall motion, the local fluid velocity assumes magnitudes lower than the lid velocities, as the moving lid experiences maximum lid motion. However, in the case of antiparallel oscillating wall motion, the local fluid velocity (at $t = 0.2$T) exceeds the magnitude of the instantaneous lid velocity. This observation can be reported in the top and bottom halves of the cavity, as the walls move in the opposite directions with same lid velocities. A similar observation was initially described in an oscillating square cavity by Mendu and Das [35]. Another significant importance in the oscillating wall motion lies in the presence of several local extremum due to the periodic motion of the cavity (seen from the $v$-centreline velocity plots). These extrema indicate repetitive changes in the magnitude and direction of the velocities, which signify the presence of complex vortices, thus causing enhanced mixing of the fluid. This is also substantiated by the number of vortex cores captured in the streamline patterns in these oscillating motions. Since the repetitive velocity variation is absent in the uniform wall motion, it is advisable to induce oscillating movements for mixing applications.

Akin to the uniform wall motion, the velocity components (both $u$ and $v$) attain the value of zero at the centre of the cross-shaped cavity in the oscillating motions too. Since the top and bottom walls have same lid motions (with same magnitude, but opposite directions), the centreline velocity profiles are skew-symmetric. Additionally, the velocity profiles in the first and second halves are mirror images of each other, similar to the streamline patterns. This implies reversal of the fluid motion, as the velocities in the second half-cycle assume the values corresponding to the first half-cycle, observed in the variation of a cosine wave.

For brevity, the streamline plots for other Reynolds numbers and oscillating frequencies have been captured only at $t = 0.2$T, 0.3T and 0.4T time instants. Akin to the uniform wall motions considered earlier, the simulations have been repeated for $Re = 200$ to 1000. At a fixed frequency of $\omega = 2\pi/6$, additional vortices are visible near the bounding walls for $Re = 500$ and 1000 in comparison to $Re = 200$, apart from the secondary vortices near the centre of the cavity domain as seen in Fig. 29. Additionally, the size and strength of these primary vortices seem to diminish due to their shrinkage caused by the formation of other vortices.

To observe the effect of oscillating frequencies, simulations were performed for a low and high frequency : $\omega = 2\pi/6$ and $4\pi/3$. At the high oscillating frequency of $4\pi/3$, formation of vortices seem to be concentrated only at the top and bottom halves of the cavity domain (generated due to the moving lid motion) or close to the bounding walls. However, the rate of formation of the vortices near the central portion of the fluid domain decreases. This indicates that the penetration of the fluid mass into the cavity domain at high frequencies diminishes, when compared with high frequencies. A similar interpretation can be inferred from the centreline velocity profiles explained later.

As Reynolds number increases, the $u$-velocity profiles show the restriction of the fluid mass below the lid (thinning of the width of velocity profiles). A similar thinning of the $v$-velocity profiles at the centreline portion of the fluid can be observed. This observation thus reports that low Reynolds numbers are preferable for high mixing phenomenon for antiparallel motion. On a similar note, increasing the oscillating frequency at fixed Reynolds numbers causes similar thinning of the velocity profiles. Thus, low oscillating frequencies are preferable for mixing phenomenon in the case of antiparallel motion. See Figs. 30–32.

### 3.4. Cross shaped cavity with parallel oscillating wall motion

This section discusses the flow in a double sided cross-shaped cavity with parallel oscillating wall motion using TRT model of LBM. Geometry and boundary conditions of the cavity are shown in Fig. 33. The direction of the top and bottom wall movements are chosen in same directions so that interesting fluid flow patterns may be observed inside this cross-shaped cavity.

Fig. 34(a)–(l) show that the streamlines at each time instant are symmetric with respect to the horizontal axis similar to the case of parallel uniform wall motion. Initially (at $t = 0.2$T), the cross-shaped cavity is primarily dominated by a pair of primary vortices generated due to the lid motion. Additionally, two pairs of vortices in the left and right halves of the cavity are also observed, which tend to enlarge in size with the passage of time. As time progresses to 0.3T, another pair of counterclockwise vortices close to the moving lids is observed, which is chiefly generated due to the no-slip boundary conditions at the wall. As the lids tend to move backward (in the first half of the cycle), these pair of vortices get merged with the vortices previously generated at the left half of the cavity, causing the primary vortices to gradually shrink. At the end of the half cycle (at $t = 0.5$T), the pair of counterclockwise vortices occupy the top and bottom half regions of the cavity, along with a pair of secondary vortices located in the left half of the fluid domain. The same vortex motion is observed in the second half of the cycle, due to the periodicity of the motion.

Fig. 35(a) and (b) show the centreline $u$-velocity profiles, with complex variation of the fluid velocities. This complex variation is substantiated by the presence of several local extremum, due to the periodic motion of the cavity. However, the centreline $v$-velocity (from Fig. 36) is almost negligible due to the formation of shear

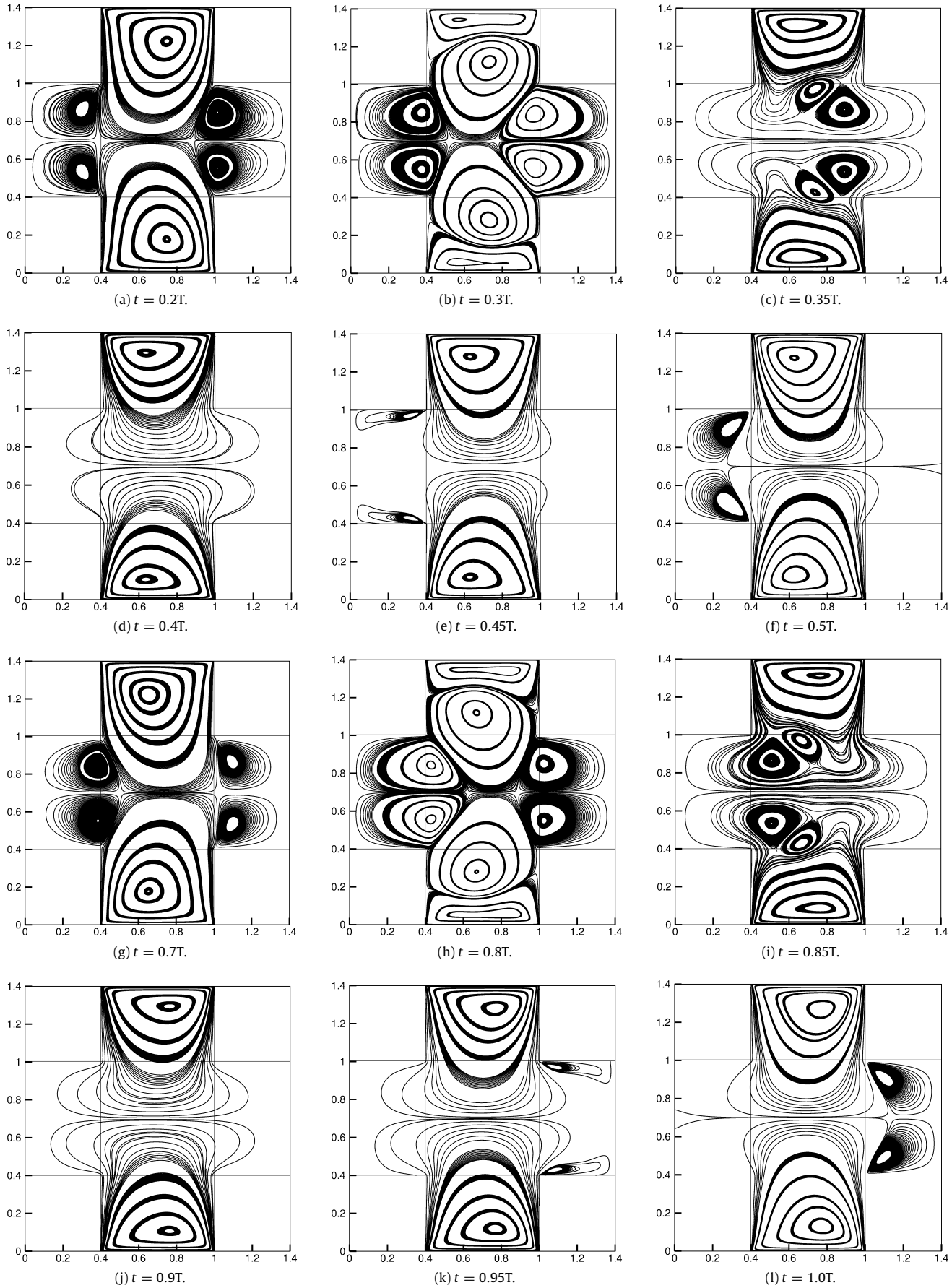

(a) $t = 0.2$T. (b) $t = 0.3$T. (c) $t = 0.35$T.

(d) $t = 0.4$T. (e) $t = 0.45$T. (f) $t = 0.5$T.

(g) $t = 0.7$T. (h) $t = 0.8$T. (i) $t = 0.85$T.

(j) $t = 0.9$T. (k) $t = 0.95$T. (l) $t = 1.0$T.

**Fig. 34.** Streamline plots during the cycle for double sided parallel oscillating wall motion at $Re = 200$, $\omega = 2\pi/6$.

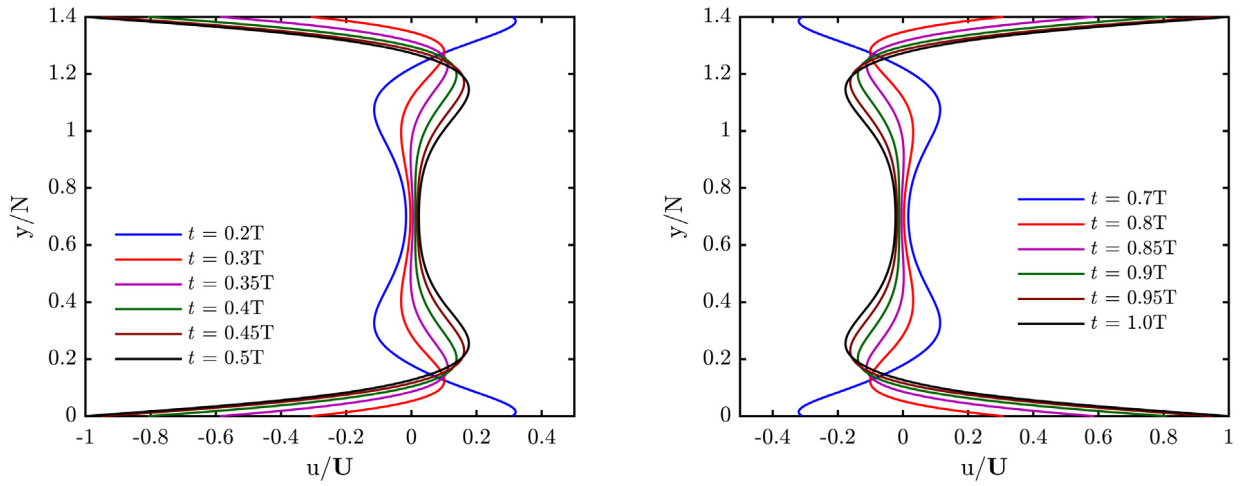


(a) First half of the cycle. (b) Second half of the cycle.

**Fig. 35.** Centreline $u$-velocity profiles for double sided parallel oscillating wall motion during (a) First half of the cycle and (b) Second half of the cycle.

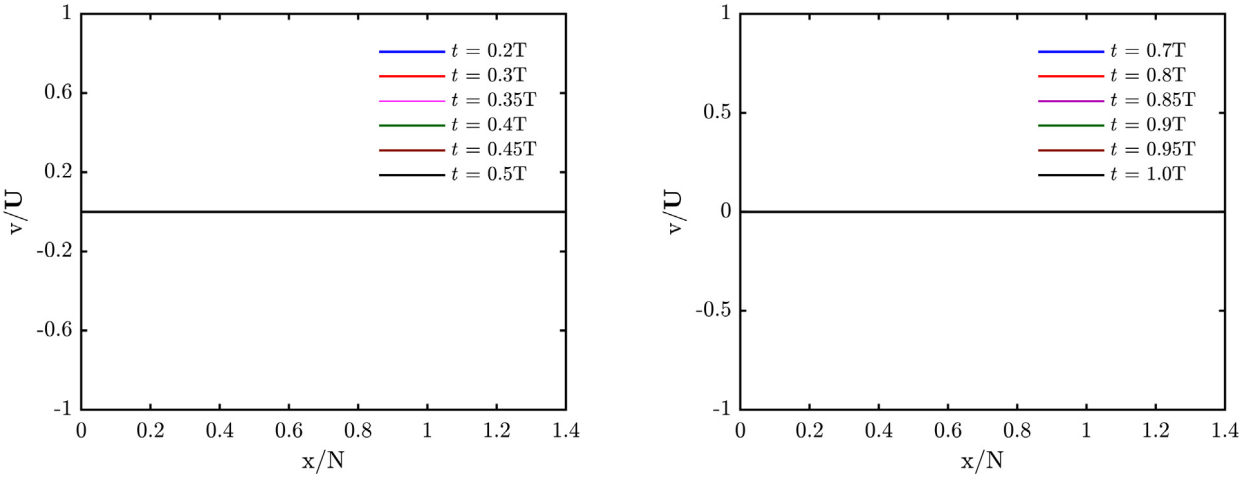


(a) First half of the cycle. (b) Second half of the cycle.

**Fig. 36.** Centreline $v$-velocity profiles for double sided parallel oscillating wall motion during (a) First half of the cycle and (b) Second half of the cycle.

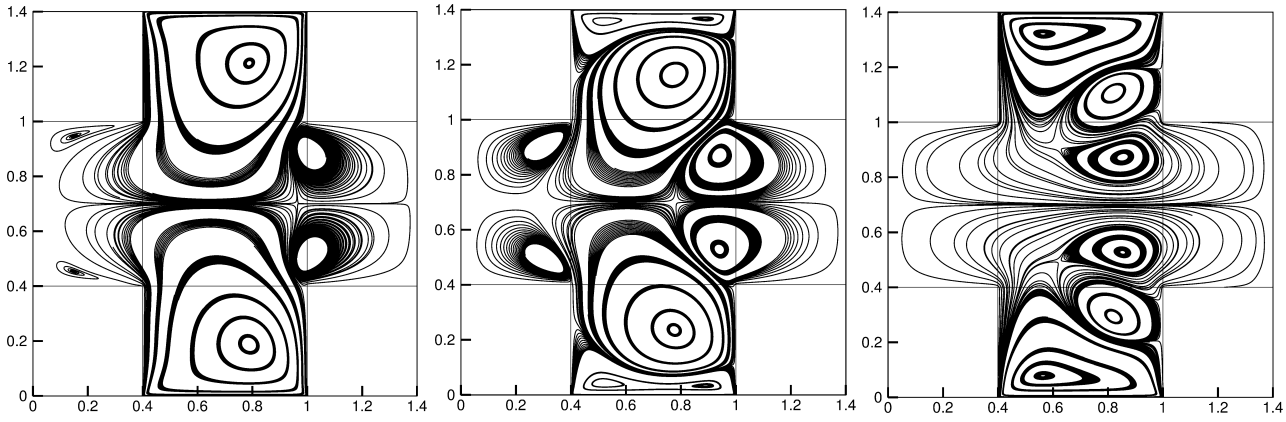

(a) $Re = 500$.

**Fig. 37.** Streamline plots for double sided parallel oscillating wall motion at $t = 0.2$T (left), $t = 0.3$T (centre) and $t = 0.4$T (right) for various Reynolds numbers at $\omega = 2\pi/6$.

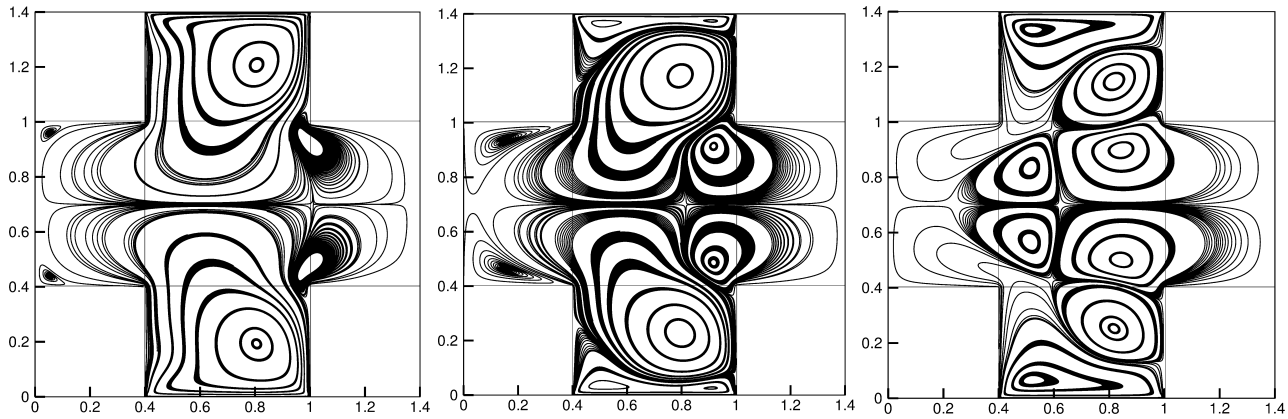

(b) $Re = 1000$.

**Fig. 37.** (*continued*)

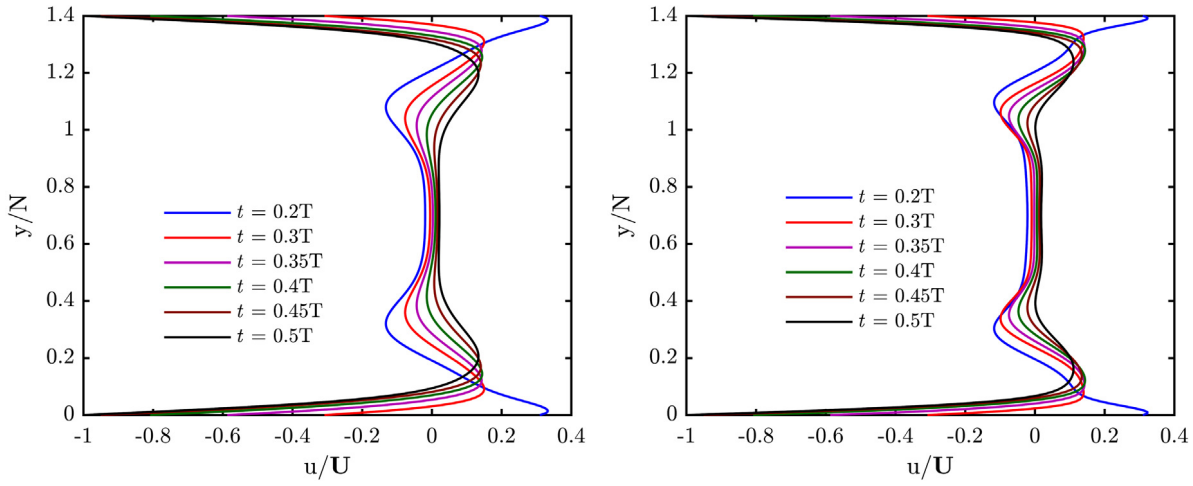


**Fig. 38.** Centreline velocity profiles for double sided parallel oscillating wall motion during the first half of the cycle for $Re = 500$ (left) and $Re = 1000$ (right) at $\omega = 2\pi/6$.

layer at the centre of the cavity. A similar formation of the shear layer was observed earlier in the case of uniform parallel motion. Moreover, the centreline velocity profiles are symmetric, similar to the streamline patterns due to the motion of the walls in the same direction.

For an increase in the oscillating frequency, the size and strength of the vortices in the entire fluid domain at parallel oscillating wall motion seem to diminish as seen in Fig. 37. However, in the case of antiparallel oscillating wall motion, the formation of wall eddies and vortices near the moving walls increases, though in the central cavity portion decreases. This can be substantiated by the shrinkage of primary vortices with subsequent tendency of other vortices to get merged with the former (as seen in Fig. 39). Thus, this necessitates the usage of low oscillating frequencies for optimum fluid mixing even in the case of parallel oscillating motions. On a similar note, the thinning of the centreline velocity profiles (Figs. 38 and 40) also supports this statement. For optimum mixing phenomenon, a low Reynolds number is preferable in the case of parallel oscillating wall motion too, for a similar reason as explained earlier.

## 4. Conclusions

A complex problem of cross-shaped double sided cavity with uniform and oscillating wall motion is introduced in the context of benchmarking, using mesoscopic lattice Boltzmann method. Initially, results are obtained for the antiparallel uniform wall motion of the cross-shaped double-sided cavity and validated with the published literature. With this belief, it has been extended to parallel uniform and oscillating wall motions of the cavity. It is believed that these four pertinent fluid flow problems have the potential to become equally popular as other benchmark cavity problems like single sided square cavity, double-sided square cavity, natural convection in the cavity etc. This manuscript also lists a variety of interesting fluid flow features including vortex dynamics, symmetry and skew-symmetry of the streamlines which cannot be verified from existing benchmark problems. Qualitative flow features such as streamline patterns, velocity profiles, pressure and vorticity contours are also depicted for various Reynolds numbers at different oscillating frequencies. Quantitative results of 2D vortex core positions are also tabulated for a better understanding of fluid motion. Three dimensional boundary layer effects are also studied

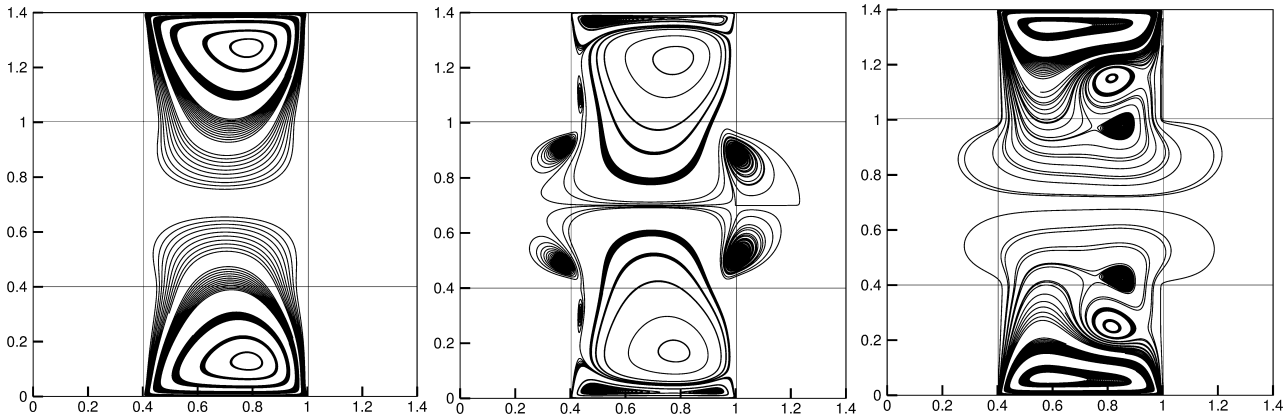

(a) $Re = 200$.

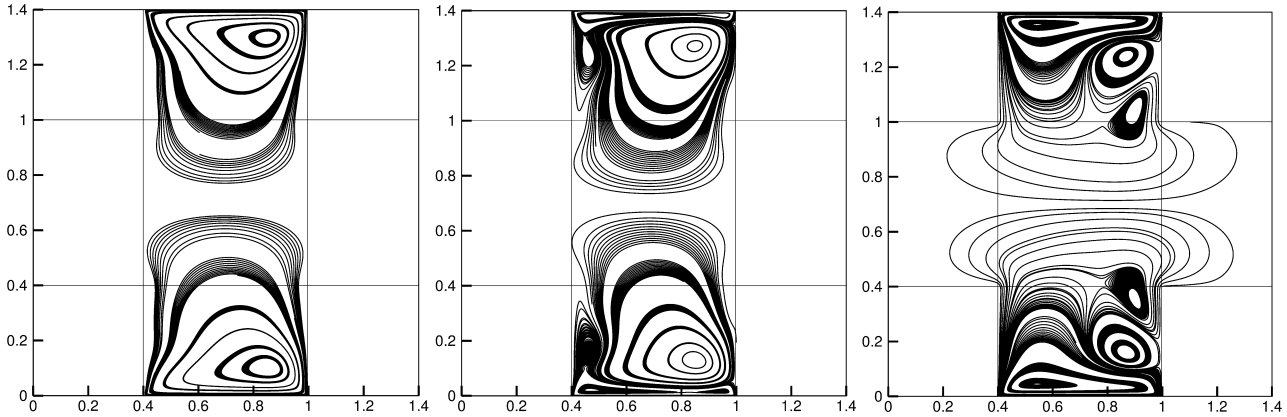

(b) $Re = 500$.

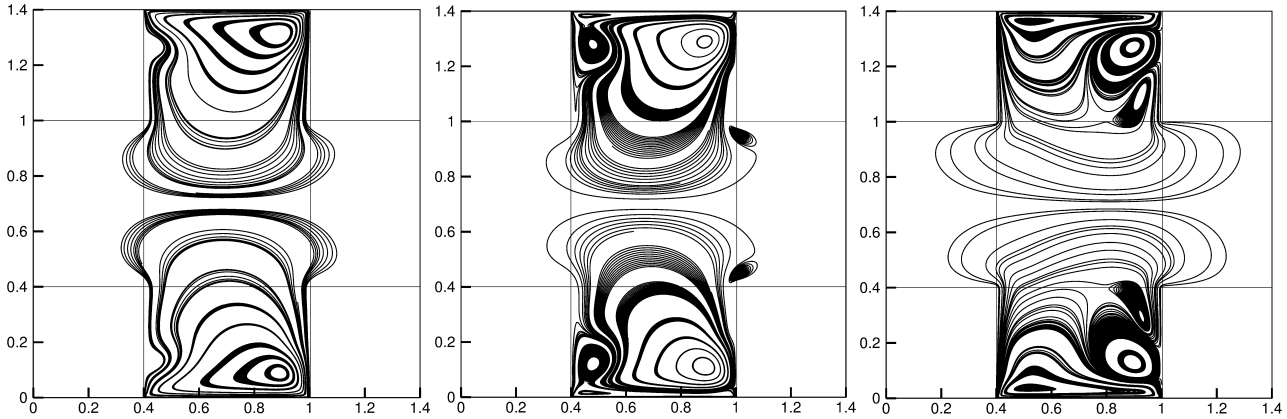

(c) $Re = 1000$.

**Fig. 39.** Streamline plots for double sided parallel oscillating wall motion at $t = 0.2$T (left), $t = 0.3$T (centre) and $t = 0.4$T (right) for various Reynolds numbers at $\omega = 4\pi/3$.

in the case of low Reynolds numbers. Studies carried out in the case of oscillating wall motions show the importance of using low Reynolds numbers and low oscillating frequencies for optimum fluid mixing phenomenon in this particular cavity configuration. This has been verified by capturing streamline plots at various time instants and through the centreline velocity profiles. On a practical scenario, a combination of low to moderate Reynolds number (100–500) with a low oscillating frequency ($\omega = 2\pi/6$) depending on the application will suffice. This has been found to render better mixing than uniform wall motions. Additionally, the qualitative and quantitative results of this cavity configuration presented in this work will make it easier for the future researchers to compare their results.

## Acknowledgements

The authors thank the anonymous reviewers for their constructive suggestions and comments, in improving the contents of the manuscript. The computing resources utilized at the Computational Fluid Dynamics Laboratory, Department of Mechanical Engineering at National Institute of Technology Karnataka, Surathkal are also deeply acknowledged.

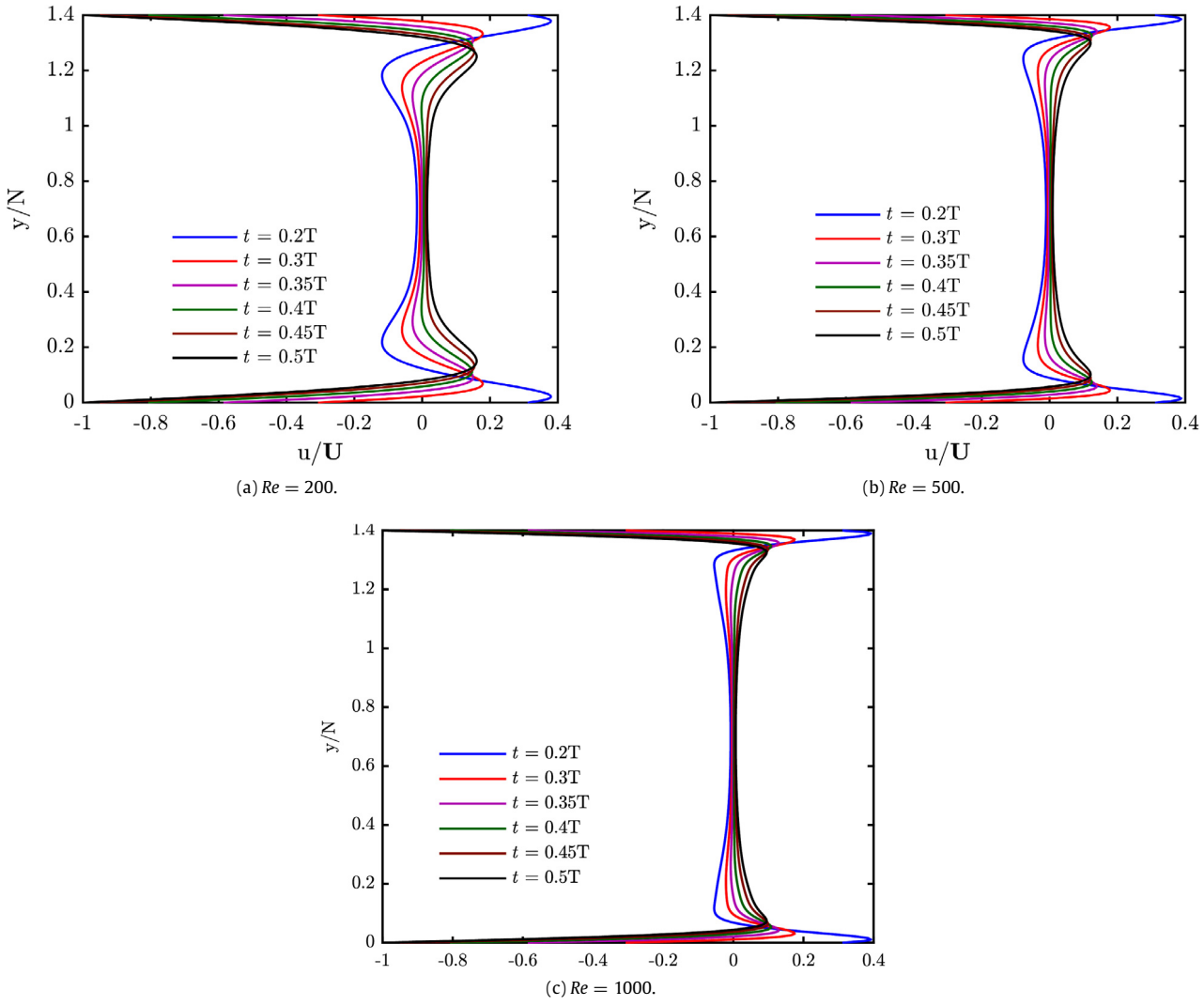


(a) $Re = 200$. (b) $Re = 500$.

(c) $Re = 1000$.

**Fig. 40.** Centreline velocity profiles for double sided parallel oscillating wall motion during the first half of the cycle for various Reynolds numbers at $\omega = 4\pi/3$.

## References


[1] S. Succi, The Lattice Boltzmann Method for Fluid Dynamics and Beyond, Oxford University Press, 2001.

[2] Y. Sone, Kinetic Theory and Fluid Dynamics, Birkhauser, Boston, 2002.

[3] D.A. Perumal, A.K. Dass, A review on the development of lattice Boltzmann computation of macro fluid flows and heat transfer, Alex. Eng. J. 54 (2015) 955–971.

[4] P.N. Shankar, M.D. Deshpande, Fluid mechanics in the driven cavity, Annu. Rev. Fluid Mech. 32 (2000) 93–136.

[5] C.K. Aidun, N.G. Triantafillopoulos, J.D. Benson, Global stability of a lid-driven cavity with through flow: flow visualization studies, Phys. Fluids A 3 (9) (1991) 2081–2091.

[6] D.A. Zumbrunnen, K.C. Miles, Y.H. Liu, Auto-processing of very fine scale composite materials by chaotic mixing of melts, Composites A 27 (1) (1996) 37–47.

[7] D.A. Perumal, A.K. Dass, Multiplicity of steady solutions in two-dimensional lid-driven cavity flows by lattice Boltzmann method, Comput. Math. Appl. 61 (2011) 3711–3721.

[8] V.Y.A. Bogatyrev, A.V. Gorin, End effects in rectangular cavities, Fluid Mech. Sov. Res. 7 (1978) 101–106.

[9] J.R. Koseff, R.L. Street, On the end-wall effects in a lid driven cavity flow, J. Fluids Eng. 106 (4) (1984) 390–398.

[10] Deliceoğlu, S.H. Aydin, Flow bifurcation and eddy genesis in an L-shaped cavity, Comput. & Fluids 73 (2013) 24–46.

[11] Deliceoğlu, S.H. Aydin, Topological Flow structures in an L-shaped cavity with horizontal motion of the upper lid, J. Comput. Appl. Math. 259 (2014) 937–943.

[12] A. Kasaeipoor, B. Ghasemi, S.M. Aminossadatti, Convection of Cu–water nanofluid in a vented T-shaped cavity in the presence of magnetic field, Int. J. Therm. Sci. 94 (2015) 50–60.

[13] M.H. Esfe, A.A.A. Arani, W.-M. Yan, A. Aghaei, Natural convection in T-shaped cavities filled with water-based suspensions of COOH-functionalized multi walled carbon nanotubes, Int. J. Mech. Sci. 121 (2017) 21–32.

[14] S. Mojumder, S. Saha, S. Saha, M.A.H. Mamun, Effect of magnetic field on natural convection in a C-shaped cavity filled with ferrofluid, Procedia Eng. 105 (2015) 96–104.

[15] T. Zhang, B. Shi, Z. Chai, Lattice Boltzmann simulation of lid-driven flow in trapezoidal cavities, Comput. & Fluids 39 (2010) 1977–1989.

[16] L. Ding, W. Shi, H. Luo, H. Zheng, Investigation of incompressible flow within $\frac{1}{2}$ circular cavity using lattice Boltzmann method, Internat. J. Numer. Methods Fluids 60 (2009) 919–936.

[17] R. Glowinski, G. Guidoboni, T.-W. Pan, Wall-driven incompressible viscous flow in a two-dimensional semi-circular cavity, J. Comput. Phys. 216 (2006) 76–91.

[18] O.R. Burgraff, Analytical and numerical studies of the structure of steady separated flows, J. Fluid Mech. 24 (1) (1966) 113–151.

[19] U. Ghia, K.N. Ghia, C.T. Shin, High-Re solutions for incompressible flow using the Navier–Stokes equations and a multigrid method, J. Comput. Phys. 48 (3) (1982) 387–411.

[20] A.B. Cortes, J.D. Miller, Numerical experiments with the lid driven cavity flow problem, Comput. & Fluids 23 (1994) 1005–1027.

[21] F. Pan, A. Acrivos, Steady flows in rectangular cavities, J. Fluid Mech. 28 (4) (1967) 643–655.

[22] H.C. Kuhlmann, M. Wanschura, H.J. Rath, Flow in two-sided lid-driven cavities: non-uniqueness, instability, and cellular structures, J. Fluid Mech. 336 (1997) 267–299.

[23] D.A. Perumal, A.K. Dass, Simulation of incompressible flows in two-sided lid-driven square cavities. Part I — FDM, CFD Lett. 2 (2010) 13–24.
[24] S. Albensoeder, H.C. Kuhlmann, Accurate three-dimensional lid-driven cavity flow, J. Comput. Phys. 206 (2005) 536–558.
[25] T.W.H. Shew, S.F. Tsai, Flow topology in a steady three-dimensional lid driven cavity, Comput. & Fluids 31 (2002) 911–934.
[26] R. Mei, W. Shyy, D. Yu, L.S. Luo, Lattice Boltzmann method for 3-D flows with curved boundary, J. Comput. Phys. 161 (2000) 680–699.
[27] C. Shu, X.D. Niu, Y.T. Chew, Taylor series expansion and least squares-based lattice Boltzmann method: three-dimensional formulation and its applications, Internat. J. Modern Phys. C 14 (2003) 925–944.
[28] S. Sriram, Abhijit P. Deshpande, S. Pushpavanam, Analysis of spatiotemporal variations and flow structures in a periodically driven cavity, J. Fluids Eng. 128 (3) (2006) 413–420.
[29] Z. Hu, et al., Fluid flow in a cavity driven by an oscillating lid by an improved incompressible SPH, Procedia Eng. 126 (2015) 275–279.
[30] R. Iwatsu, J.M. Hyun, K. Kuwahara, Numerical simulation of flows driven by a torsionally oscillating lid in a square cavity, J. Fluids Eng. 114 (2) (1992) 143–151.
[31] C.-L. Chen, C.-H. Cheng, Numerical simulation of periodic mixed convective heat transfer in a rectangular cavity with a vibrating lid, Appl. Therm. Eng. 29 (14) (2009) 2855–2862.
[32] D.Z. Noor, P.R. Kanna, M. Chern, Flow and heat transfer in a driven squarecavity with double-sided oscillating lids in anti-phase, Int. J. Heat Mass Transfer 52 (2009) 3009–3023.
[33] T. Nishimura, K. Kunitsugu, Fluid mixing and mass transfer in two-dimensional cavities with time-periodic velocity, Int. J. Heat Fluid Flow 18 (1997) 497–506.
[34] S. Takasaki, K. Ogawara, S. Iida, A study on chaotic mixing in 2D cavity flows: Effects of Reynolds number and amplitude of lid velocity, JSME Int. J. B 37 (1994) 237–241.
[35] S.S. Mendu, P.K. Das, Fluid flow in a cavity driven by an oscillating lid-asimulation by lattice Boltzmann method, Eur. J. Mech. B Fluids 39 (2013) 59–70.
[36] T.J. Chung, Computational Fluid Dynamics, Cambridge University Press, Cambridge, 2002.
[37] X. Guo, C. Zhong, C. Zhuo, J. Cao, Multiple-relaxation-time lattice Boltzmann method for study of two-lid-driven cavity flow solution multiplicity, Theor. Comput. Fluid Dyn. 28 (2014) 215–231.
[38] I. Ginzburg, F. Verhaeghe, D. d'Humieres, Two relaxation-time lattice Boltzmann scheme: About parameterization, velocity, pressure and mixed boundary conditions, Commun. Comput. Phys. 3 (2) (2008) 427–478.
[39] Y. Shao, J.S. Wu, Simulation of lid-driven cavity flows by parallel lattice Boltzmann method using multi-relaxation-time scheme, Internat. J. Numer. Methods Fluids 46 (9) (2004) 921–937.
[40] C. Shu, X.D. Niu, Y. Peng, Y.T. Chew, Taylor series expansion- and least square-based lattice Boltzmann method: an efficient approach for simulation of incompressible viscous flows, Prog. Comput. Fluid Dyn. 5 (1/2) (2005) 27–35.
[41] K. Qu, C. Shu, Y.T. Chew, An isoparametric transformation-based interpolation–supplemented lattice Boltzmann method and its application, Modern Phys. Lett. B 24 (13) (2010) 1315–1318.
[42] H.Z. Yuan, X.D. Niu, S. Shu, M. Li, H. Yamaguchi, A momentum exchange-based immersed boundary-lattice Boltzmann method for simulating a flexible filament in an incompressible flow, Comput. Math. Appl. 67 (5) (2014) 1039–1056.
[43] J.D. Vicente, D. Rodriguez, V. Theofillis, E. Valero, Stability analysis in spanwise-periodic double-sided lid-driven cavity flows with complex cross-sectional profiles, Comput. & Fluids 43 (2011) 143–153.
[44] B.B. Gogoi, J.C. Kalita, On the global instability of square and cross lid-driven cavity flows with a pure streamfunction-velocity ($\Psi - V$) approach, in: International Conference on Computer Aided Engineering, December 19–21, IIT Madras, Chennai, India, 2013.
[45] B.B. Gogoi, Global 2D stability analysis of the cross lid-driven cavity flow with a streamfunction–vorticity approach, Int. J. Comput. Methods Eng. Sci. Math. 17 (4) (2016) 253–273.
[46] Y.C. Zhou, B.S.V. Patnaik, D.C. Wan, G.W. Wei, DSC solution for flow in a staggered double lid driven cavity, Internat. J. Numer. Methods Engrg. 57 (2003) 211–234.
[47] P. Nithiarasu, C.-B. Liu, Steady and unsteady incompressible flow in a double lid driven cavity using the artificial compressibility (AC)-based characteristic-based split (CBS) scheme, Internat. J. Numer. Methods Engrg. 63 (2005) 380–397.
[48] J.C. Kalita, B.B. Gogoi, Global two-dimensional stability of the staggered cavity flow with an HOC approach, Comput. Math. Appl. 67 (2014) 569–590.
[49] P.M. Tekić, J.R. Radenović, N.Lj. Lukić, S.S. Popović, Lattice Boltzmann simulation of a two-sided lid driven flow in a staggered cavity, Int. J. Comput. Fluid Dyn. 24 (9) (2010) 383–390.
[50] D.A. Perumal, A.K. Dass, Application of lattice Boltzmann method for incompressible viscous flows, Appl. Math. Model. 37 (2013) 4075–4092.
[51] D. Yu, R. Mei, L.S. Luo, W. Shyy, Viscous flow computations with the method of lattice Boltzmann equation, Prog. Aerosp. Sci. 39 (2003) 329–367.
[52] I. Ginzburg, D. d'Humiéres, A. Kuzmin, Optimal stability of advection–diffusion lattice Boltzmann models with two relaxation times for positive/negative equilibrium, J. Stat. Phys. 139 (6) (2010) 1090–1143.
[53] Q. Zou, X. He, On pressure and velocity boundary conditions for the lattice Boltzmann BGK model, Phys. Fluids 9 (6) (1997) 1591–1598.
[54] J.M. Pérez, A. Aguilar, V. Theofilis, Lattice Boltzmann methods for global linear instability analysis, Theor. Comput. Fluid Dyn. (ISSN: 1432-2250) (2016) 1–22.
[55] D.A. Perumal, A.K. Dass, Simulation of incompressible flows in two-sided lid-driven square cavities. Part II — LBM, CFD Lett. 2 (2010) 25–38.
[56] D.A. Perumal, Lattice Boltzmann simulation of laminar flow in a three-dimensional two-sided lid-driven cavity, World J. Modell. Simul. 9 (4) (2013) 277–288.